Metallic Flame-Sprayed Coatings as Anti-Icing and De-Icing Systems for Wind Turbines

by

Adrian Lopera

A thesis submitted in partial fulfillment of the requirements for the degree of

Master of Science

Department of Mechanical Engineering

University of Alberta

© Adrian Lopera, 2015

ABSTRACT

Ice accretion is a problem that affects the performance and safety of structures that are exposed to cold weather environments. In wind energy production, a constantly growing industry, ice accretion has been found to decrease the performance, produce mechanical failures, and decrease the safety of wind turbines in cold climates. The development of methods to decrease and mitigate the effects of ice accretion in the performance, longevity, and safety of wind turbines has been the main objective of many studies. In this thesis, flame-sprayed nickel-chromium-aluminum-yttrium (NiCrAlY) and nickel-chromium (NiCr) coatings were deposited on fiber-reinforced polymer composites (FRPC). Electrical current was applied to the coatings to increase the surface temperature by way of Joule heating. The performance of the coatings as heating elements was tested under different cold environment conditions. In addition, heat transfer models were developed to predict the heating and melting times of ice during the de-icing process. It was found that the coatings were effective heating elements for melting accumulated ice on polymer composite structures that were exposed to cold environments. The results of a finite length-scale model and its agreement with experimental data suggest that a heat conduction model may be applied to free boundary problems to predict phase change phenomena induced by thermal-sprayed coatings.

ACKNOWLEDGMENTS/AGRADECIMIENTOS

I would like to express my endless gratitude to my friend and supervisor Dr. André McDonald. This thesis and my graduate studies would not be possible without his indefatigable and encouraging supervision. Thanks to his company and advice, my master's degree was a pleasant learning experience that prepared me keep pursuing my academic career.

I would like to thank all my colleges and friends from room MecEng 6-25. Particularly, I want to thank Rael Gonzalez and Sayed Hossein Ashrafizadeh, their experience and advice have helped me with both technical and administrative tasks. Having them around during these two years has encouraged me to be a more proactive graduate student.

Finalmente quiero agradecer a mis familiares y amigos, que desde la distancia o la cercanía, me han alentado y compartido mis triunfos. Quiero dar infinitas gracias a mis padres: Gloria y Fernando, por haber inculcado en mí la honestidad, el amor y la perseverancia, valores que han hecho de mí la persona que soy. A mi hermano, mi mejor amigo, Sebastian, quiero agradecer por servirme de ejemplo y compañía durante toda una vida de juegos, peleas, travesuras, miradas que no necesitan palabras, videojuegos, libros y trasnochadas. A Esnedita, tías y abuelas: Elvira y Gabriela, por servir de madres en cada día de mi vida. Finalmente, a mis grandes amigos y amigas: Lina, Freddy, Carlos, Juan David, Cynthia, Susana, Linda, Cora, Nikki y Shaina, por ser parte de este viaje.

We cannot hope to build a better world without improving the individual.
Toward this end, each of us must work for his own highest development,
accepting at the same time his share of responsibility in the general life of humanity,
our particular duty being to aid those to whom we think we can be most useful.
-Marie Curie

In memory of my paternal grandparents:

Gabriela and Manuel

TABLE OF CONTENTS

Abstract ..... *ii*

Acknowledgments/Agradecimientos ..... *iii*

List of figures ..... *vii*

List of tables ..... *ix*

Nomenclature and abbreviations ..... *x*

Symbols ..... *x*

Greek symbols ..... *xi*

Subscripts ..... *xii*

Abbreviations ..... *xiii*

1. Introduction *1*

1.1. Wind energy in cold environments *1*

1.2. Anti- and de- icing systems (ADIS) *6*

1.2.1. Anti-icing systems *6*

1.2.2. De-icing systems *7*

1.2.3. Modeling of ADIS *8*

1.3. Fiber-reinforced polymer composites (FRPC) *9*

1.4. Thermal spray process *10*

1.5. Objectives *14*

1.6. Thesis organization *14*

2. Experimental method *15*

2.1. Substrate preparation *15*

2.2. Coating deposition *17*

2.3. Coating and substrate characterization *19*

2.4. Electrical characterization *22*

2.5. Joule heating tests *22*

2.6. De-icing tests *24*

3. Mathematical model *27*

3.1. Heating ice *27*

3.2. Melting of ice of finite thickness *32*

4. Results and discussion *39*

4.1. Coating characterization *39*

4.2. Substrate characterization *43*

4.3. Electrical characterization *45*

4.4. Joule heating test under free convection conditions *49*

4.5. Joule heating test under force convection conditions *57*

4.6. De-icing test and model validation *64*

4.6.1. Heating of the ice and frpc sample *64*

4.6.2. Melting of the ice *70*

5. Conclusions *77*

6. Future work and recommendations *80*

7. References *82*

LIST OF FIGURES

Figure 1: Evolution of wind turbine diameter and power in the last 30 years……..2

Figure 2: Ice accretion on wind turbine blade…….. 4

Figure 3: Schematic of flame spraying process…… 12

Figure 4: FRPC ply after curing process…….. 16

Figure 5: Typical FRPC plate with copper terminals and sand-epoxy layer…… 17

Figure 6: Equipment used in the deposition of the coatings…….19

Figure 7: Experimental assembly for electrical characterization and Joule heating tests……23

Figure 8: Experimental air duct assembly…… 24

Figure 9: Schematic of the water dispensing system……25

Figure 10: Energy balance of ice control volume……...29

Figure 11: Schematic of melting of a layer of ice……...32

Figure 12: **a)** Low and **b)** high magnification SEM image of a NiCr coating……40

Figure 13: **a)** Low and **b)** high magnification SEM image of a NiCrAlY coating…….42

Figure 14: Longitudinal and transverse thermal conductivity of FRCP……43

Figure 15: Voltage versus current for the **a)** NiCr and **b)** NiCrAlY coating at different temperatures……47

Figure 16: Resistance versus temperature for the NiCr and NiCrAlY coatings……48

Figure 17: Temperature profiles along NiCrAlY-coated FRPC exposed to air at **a)** 23°C, **b)** -5°C, and **c)** -25°C under free convective conditions…… 51

Figure 18: Average temperature differences across the **a)** NiCrAlY-coated and **b)** NiCr-coated FRPC samples under free convective conditions…….....55

Figure 19: Power supplied versus average temperature difference for NiCr- and NiCrAlY-coated FRPC samples under free convective conditions…….. 57

Figure 20: Temperature profiles along NiCrAlY-coated FRPC exposed to air at 23°C under forced convective conditions……. 59

Figure 21: Average temperature difference across the NiCrAlY-coated and bare, uncoated FRPC surfaces under forced convective conditions…….. 62

Figure 22: Power supplied versus average temperature difference for NiCrAlY-coated and bare, uncoated FRPC surfaces under forced convective conditions…...63

Figure 23: Transient temperature traces from the de-icing test at -15°C ambient room temperature…… 65

Figure 24: Experimental and predicted heating times of the ice at different ambient temperatures…….. 70

Figure 25: Experimental and predicted **a)** dimensional and **b)** non-dimensional melting time of the ice at different ambient temperatures…….73

Figure 26: Velocity of the liquid-solid interface at different a) applied powers and b) ambient temperatures……. 76

LIST OF TABLES

Table 1: Spray parameters for NiCr and NiCrAlY coating……18

Table 2: Properties for solid water in Eq. 8…….. 31

Table 3: Heating and melting time for ice layers at different ambient temperatures…..64

Table 4: Properties for liquid water…….. 74

NOMENCLATURE AND ABBREVIATIONS

Symbols

A	surface area (m^2)
Bi	Biot number, $\mathrm{Bi} = \frac{h\delta}{k_s}$
c_p	specific heat capacity ($Jkg^{-1}K^{-1}$)
$\dot{E}$	energy rate (W)
Fo	Fourier number, $\mathrm{Fo} = \frac{\alpha_L t}{\delta^2}$
h	heat transfer coefficient ($Wm^{-2}K^{-1}$)
I	electric current, (A)
k	thermal conductivity ($Wm^{-1}K^{-1}$)
l	substrate length (m)
ℓ	emissivity
m	mass (Kg)
P	electrical power (W), $P = VI$
Pr	Prandtl number, $\frac{c_p \mu}{k}$
q''_g	heat flux due to Joule heating (Wm^{-2})

r coefficient of determination

R electrical resistance (Ω)

Re Reynolds's number, $\mathrm{Re} = \dfrac{ul}{\nu}$

T temperature (°C)

t time (s)

u free stream air velocity (ms^{-1})

V voltage (V)

x position (m)

x_i location of liquid-solid interface (m)

Greek Symbols

α thermal diffusivity (m^2s^{-1})

δ thickness of ice (m)

ε electrical resistivity (Ωm)

Γ function dependent on t, only

Δ time rate of change

θ non-dimensional temperature, $\theta = \dfrac{T_f - T_\infty}{T_f}$

λ separation constant (m^{-1})

λ	non-dimensional constant
μ	dynamic viscosity ($kgm^{-1}s^{-1}$)
v	kinematic viscosity (m^2s^{-1})
ρ	density (kgm^{-3})
Φ	function dependent on x, only
X	function dependent on x, only
Ψ	function dependent on x and t
$\hbar$	latent heat of fusion (Jkg^{-1})
∞	ambient
ϖ	Stefan-Boltzmann constant, 5.6703×10^{-8} $Wm^{-2}K^{-4}$
σ	volume fraction
ζ	thickness of FRPC sample (m)

Subscripts

A	air
eff	effective
f	fusion
F	FRPC substrate
h	heating
i	initial

in	in
L	liquid phase
m	matrix
n	number
o	out
R	radiation
r	reinforcement, fiber
s	solid phase

Abbreviations

ADIS	Anti- and De- Icing Systems
BSE	Backscattering Electron
EDX	Energy-Dispersive X-ray
FMR	Flow Meter Reading
FRPC	Fiber Reinforced Polymer Composite
NiCr	Nickel-20% wt. Chromium
NiCrAlY	Nickel-Chromium-Aluminum-Yttrium
SEM	Scanning Electron Microscope
SOD	Stand-Off Distance

1. INTRODUCTION

1.1. WIND ENERGY IN COLD ENVIRONMENTS

Wind energy is a renewable energy source, with no significant greenhouse gas emissions, that is produced by transforming the kinetic energy present in the wind into mechanical power [1, 2]. The transport of air masses in wind currents is generated by differential solar heating of air layers, which produces differences in air density and pressure, resulting in air currents with high kinetic energy [2]. The transformation of the energy in the wind into electrical power is achieved by using wind turbines, machines that comprise a rotor element, which transforms the energy in the wind into rotation, and an electrical generator that transforms the rotation into electrical energy. Other components include, structural parts, sensors that measure environment conditions such as wind velocity, wind direction, temperature and humidity, and actuators that assist in orienting the rotor in the direction of higher wind velocity [3]. The fabrication and installation of wind turbines is considered to be a well-developed industry that produces turbines from 400 W to 7.5 MW output energy with rotors that can be as large as 170 m in diameter [1, 2, 4]. Figure 1 shows the evolution of the wind turbine diameter and power in the last 30 years, providing an idea of the growth of the wind energy industry.

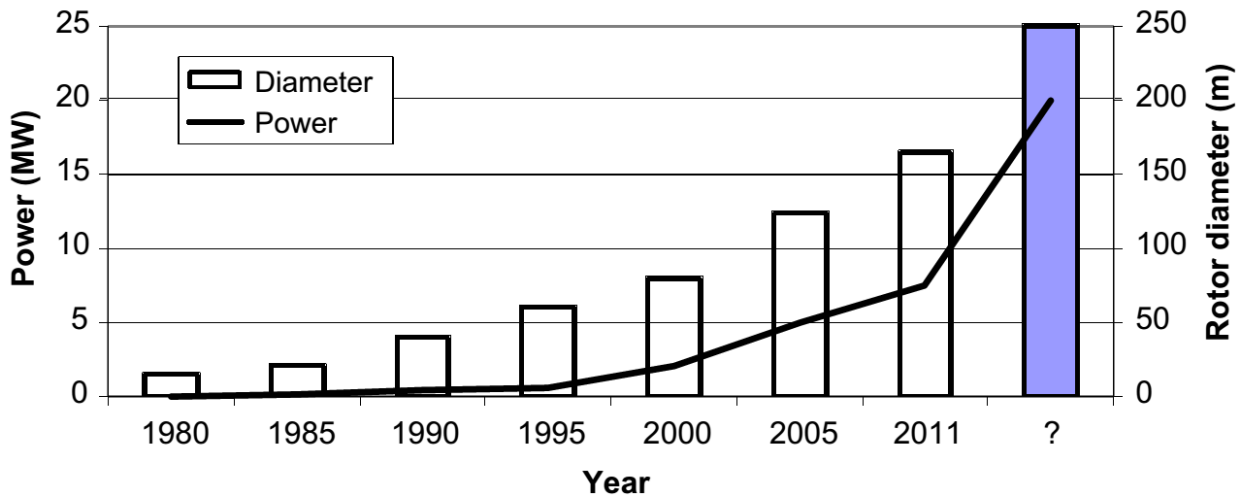

Figure 1: Evolution of wind turbine diameter and power in the last 30 years [2]

The production of wind energy has shown a fast growth in the last decade. The world-wide energy production by means of wind energy has increased from 6 GW in 1996 to 369.6 GW in 2014 and is expected to reach 666 GW by 2019 [4–6]. This fast development and the increasing demands of electricity have required the exploration of new locations for the installation of wind turbines. For instance, high altitudes and latitudes, where the air velocity is higher and the climate colder, are locations under constant exploitation to place wind turbines given that the energy production is significantly higher [1, 7, 8]. In low-temperature climates, wind turbines have been found to present about 10% more potential of electricity production than warm climates because the air density is higher in cold climates which leads into higher kinetic energy in the air currents [1, 8]. Wind energy in cold environments has been estimated to be more than 20% of the wind energy that is world-wide produced [7]. In northern countries such as Canada, a total of 1,871 MW was installed in five provinces during 2014, representing the 6th highest word-wide power capacity installation during 2014. Most of this growth was

centered in Ontario (999 MW), followed by Quebec (460 MW) and Alberta (351 MW). By the end of 2014, Canada had a total of 9,694 MW of installed wind energy capacity, supplying approximately 5% of Canada's electricity demand [5]. This accelerated growing was common in other northern countries such as United Kingdom, Sweden, United States of America and Finland in 2014.

Structures that are located in cold climates usually face the formation and accumulation of ice, commonly referred to as ice accretion [9–11]. Particularly, ice accretion affects the airfoils of airplanes (the wings) and wind turbines (the blades, Fig. 2), by decreasing their performance, safety, and durability. In planes, icing during flight produces a significant threat to safety, representing around 9% of large-scale safety accidents of aircraft during flights [12, 13]. Ice accretion has been found to be detrimental to the overall turbine performance, longevity, and safety during operation [1, 10, 14, 15]. In addition, ice accretion has produced mechanical and electrical failures, errors in the measurement of temperature, humidity and wind velocity, overproduction, and power losses up to 50% [1, 14, 16, 17]. These problems may occur for over as much as 6 months of a year [7]. For instance, the severe accumulation of ice has led to the complete shut-down of turbines in operation, resulting in significant energy losses. In Sweden, for instance, 92% of the turbine full-stop events registered between 1998 and 2003 were directly related with ice accretion [1, 15]. In other cases, ice accretion has been found to produce mass and aerodynamic imbalance of the turbine blades even in its early stages. Jasinski *et al.* [15] found that even light formations of ice on the surface can increase the surface roughness which produces an increase in the drag coefficient, yielding a reduction of the produced power. Mass and aerodynamic imbalances will cause higher fatigue and dynamic loads and increase the

excitation of edgewise vibrations [7, 8, 14, 18]. Furthermore, the formation of ice represents a safety issue as ice could be thrown at high velocity and high altitude, resulting in a threat to the safety when wind turbines are located near to borders public roads, housing, power lines, and shipping routes [1, 7]. Despite all the drawbacks caused by difficult weather conditions that were mentioned above, there is an increasing interest in the production of wind energy in both, high altitude and cold environments, given its potential higher power production as consequence of lower air densities and higher wind velocities. Therefore, finding methods to avoid and mitigate the effect of ice accretion is necessary for the energy industries since it would increase the safety and performance of equipment.

Figure 2: Ice accretion on wind turbine blade [1]

The formation of ice in wind turbines and other structures occurs under different conditions that result in the formation of different types of ice. The two main types of ice that have been found to affect wind turbines are: in-cloud and precipitation ice, which can be further divided into rime and glaze ice, and wet snow and freezing rain, respectively [1, 14, 19].

In-cloud ice accretion occurs when super-cooled water droplets that are suspended in the air (similar to mist), at temperatures below -20°C, freeze upon impact with a surface. The size of the droplets and the ambient temperature would affect whether the ice is rime or glaze type. Rime is formed when the heat of a droplet of ice is removed quickly due to the low temperature of the surface and high wind velocities [1, 19]. As result of the quick heat loss in the droplets of water, they solidify upon impact and accumulate on the surface, resulting in a porous layer of ice that comprises disk-shaped water splats and air voids. On the other hand, glaze ice is formed when the thermal energy removed after impact is not enough to immediately freeze the droplets of ice and a portion of them remain as liquid water which finally solidifies, generating clear ice with low air content and higher density which make glaze ice significantly more difficult to remove than rime ice [1, 14, 19].

Precipitation ice accretion occurs when wet snow crystals with a portion of liquid water, at temperatures between 0°C and -3°C, impact a surface at temperature below 0°C and bind together, covering the surface with a low-density. In addition, precipitation icing occurs when rain, at temperatures close to 0°C, impacts a surface that is at temperatures below 0°C and

freeze [1]. The study of the formation of the different types of ice provides more information about the nucleation of ice in that contribute in the design of method to avoid ice accretion [1].

1.2. ANTI- AND DE- ICING SYSTEMS (ADIS)

The growing demand for wind energy in cold environments requires the development of methods to both avoid and mitigate the detrimental effects of ice accretion on the performance, longevity and safety of wind turbines. Ice mitigation systems comprise two groups, (1) based on anti-icing methods that avoid the formation of ice, and (2) based on de-icing methods that remove and avoid the accumulation of the ice [1, 14].

1.2.1. Anti-icing systems

Several studies have been focused on designing and assessing systems to avoid the formation of ice on blades and other components of wind turbines. These systems include the implementation of special paintings, air layers, or microwave devices to avoid ice growth. For instance, Antonini *et al.* [19] tested the effect of different hydrophobic surfaces in the formation of ice over the surface of airfoil-shaped plates that were equipped with electrical resistive heaters. The samples were exposed to cold ambient temperature, inside a wind tunnel that was equipped with a water spraying system that simulated light and heavy icing conditions. The wettability and water-surface interaction of different materials, including untreated-aluminum (Al), poly-methyl-methacrylate (PMMA)-covered, and Teflon® (DuPont™)-covered etched aluminum, were tested. The results showed that the application of a hydrophobic paint allows a significant reduction of the power supplied to the heating elements to keep the sample surface

above freezing point, avoiding the formation of ice. Other systems include using black painting to capture sun radiation which would keep the blades warm [20], and microwave heaters to keep the temperature of the blades slightly above 0°C [14, 21]. Similarly to hydrophobic surfaces and other methods, black painting and microwaves were not found to be sufficiently effective in avoiding ice accretion.

These anti-icing systems have inherent problems that make their mass production unviable [1, 14]. For instance, several studies have shown that icing prevention on wind turbine blades by using just special (hydrophobic or black-colored) paintings is not possible given that they were found to be not truly ice-phobic under field conditions [14]. Another disadvantage is that ice accretion would occur in particular spots where water accumulates or the anti-icing systems are less effective, generating unsymmetrical accretion leading to load instability [22]. In addition, paintings become porous overtime and lose their ability to adhere to the blade surface [7]. These problems have made the mass production of most of the anti-icing system not viable.

1.2.2. De-icing systems

Active de-icing systems that mitigate the adverse consequences of ice accretion on the surface of wind turbine blades, have been developed [8, 10, 13]. For example, some of these systems have implemented warm air that is blown into each blade to increase the temperature of the structure, producing the detachment of the ice [14, 23]. Warm air has been successfully implemented in an 850 kW wind turbine, consuming approximately 1% of the total electricity produced in heating and circulating the air [14, 24]. However, this method consumes a

significant amount of energy during operations at high speed winds and low temperatures. In addition, given that polymer-based composites that are used in the fabrication of wind turbine blades are insulators, air at higher temperatures is required in order to increase the temperature across the composite material, resulting in high power consumption [24]. Other de-icing methods include heating elements that are embedded or laminated in the blade structures [7, 14, 25]. The heating elements may be wires or plates that are located at the leading edge of the blades. Depending on the power production of the turbine, the heating elements can consume between 1% and 15% of the energy produced by the turbine [14, 17]. These methodologies have inherent problems, which include positioning of the heating wires in the blade to avoid potential structural issues and the occurrence of hot spots that could result in areas of the surface devoid of ice accumulation, and other areas with ice accumulation as observed by Mohseni, *et al*. [25]. Research on solving these problems is required to produce reliable de- and anti- icing systems that can be commercially produce for wind turbines that face ice accretion.

1.2.3. Modeling of ADIS

The modeling of de- icing systems based on vibrations has been previously conducted. For instance, Habibi, *et al*. [26] implemented finite element method (FEM) simulations in the design of a dual de-icing system that combined high-power ultrasonic waves and low-frequency forced vibrations. FEM simulations were used to optimize the design of the anti-icing system elements and investigate their effect on the structural integrity of the wind turbine blades. In the simulation of heating elements for Fiber Reinforced Polymer Composites (FRPC), Zhu, *et al*. [27] presented a numerical model for a FPRC curing process that was accelerated with heating

mats. This model could predict the temperature distribution inside the composite and estimate the curing time in terms of dimensionless groups. In addition, Lamarre, *et al*. [18] modeled the temperature distribution and thermal stresses in an iron-based wire flame-sprayed heating element on a titanium substrate. Other general models on phase change that involve melting have been developed [28, 29]. In particular, Cleland, *et al*. [29] has implemented numerical methods in the prediction of the freezing and thawing for regular and irregular shaped objects. The validation of the numerical methods was done by comparing the model results against several experimental data. This study proved that numerical methods used are valid for the two- and three- dimensional shapes with some particular exceptions. Nevertheless, there has been limited research on the theoretical modeling of metal coatings as de-icing elements for FRPC components.

1.3. FIBER-REINFORCED POLYMER COMPOSITES (FRPC)

Composite materials have gained popularity in the production of high performance products that require materials with low density (low weight) and improved mechanical properties. Structures in the aerospace industry (tails, wings, and fuselages), boat manufacturing, automobile, communications, and energy production industries, are examples of the wide range of applications of composite materials. In the wind energy industry, fiber-reinforced polymer composites (FRPC) are widely selected for the fabrication of wind turbine blades and other components due to their large strength and stiffness to weight ratio compared with conventional structural materials [27–30].

While FRPCs provide several mechanical benefits to wind turbine structures, their thermal properties typically do not allow them to conduct heat rapidly. Previous work has been conducted in enhancing the thermal properties of FRPC elements. Applications in heat exchangers, pipe manufacturing, electronics, civil construction, automobile, and energy generation industries have required the development of polymer-based composites with the ability of dissipating heat while providing their beneficial mechanical properties. For example, Han and Chung [31] have implemented higher manufacturing pressures and the addition of carbon-based fillers in increasing the thermal conductivity of carbon fiber-reinforced epoxy, which is usually used in aircraft radiators, an application that requires that the composite material dissipates heat rapidly [31]. Moreover, in the design and assessment of ADIS for wind turbines, it has previously been shown that the low thermal conductivity of the composite material used in manufacturing wind turbines decreases the performance of ADIS in large turbines where the FRPC materials work as insulation between the heat source and the blade surface where the ice accretion occurs [14, 24]. Therefore, the design of methods to increase the thermal conductivity and diffusivity of FRPC is required to develop ADIS based on heating elements.

1.4. THERMAL SPRAY PROCESS

Thermal spray processes are a group of rapidly growing industrial processes used in the surface modification of elements by the deposition of a layer of a material in order to protect it from surface degradation caused by high temperature, corrosion, oxidation, and/or wear. In this group of processes, thermal energy is used in heating and melting a feed stock material (powder

or wire) that is afterward propelled in the form of droplets towards a surface. The droplets deform upon impact, becoming disk-shaped splats that accumulate, forming a coating over the substrate surface [32–34]. In addition to protecting a surface, coatings can be used to improve electric, thermal, and magnetic properties of the structures upon which they are deposited [35, 36]. The wide range of applications and the versatility of this processes make it widely used in aerospace, automobile, mining, energy generation, and oil industries, among several other industries [33].

Flame spraying was the first thermal spray process that was developed. In its early development stages, oxy-acetylene-flame welding torches were modified to adapt the feeding of powder into the flame. Regardless of its long history, flame spraying is currently used in several applications mainly due to its low cost in equipment, maintenance, and consumables [33]. Flame spraying, as shown in Fig. 3, uses the energy of oxidizing and flammable gases to form a high temperature flame. During the coating deposition, small-sized particles or thin wires are partially or totally molten and accelerated by the expanding gasses towards the substrate. The small droplets of material deform upon impact with the substrate and solidify generating a layer of coating material. Oxygen-acetylene torches are the most commonly used, mixing acetylene (C_2H_2) as the main fuel in combination with oxygen to generate a combustion temperature of approximately 3160°C [33, 34]. Other torches use propane (C_3H_8), propylene (C_3H_6), hydrogen (H_2), and ethane (C_2H_4) [33, 37]. The operation temperature makes flame spraying capable of depositing a wide range of materials, including polymers, ceramics, cermets, and metals.

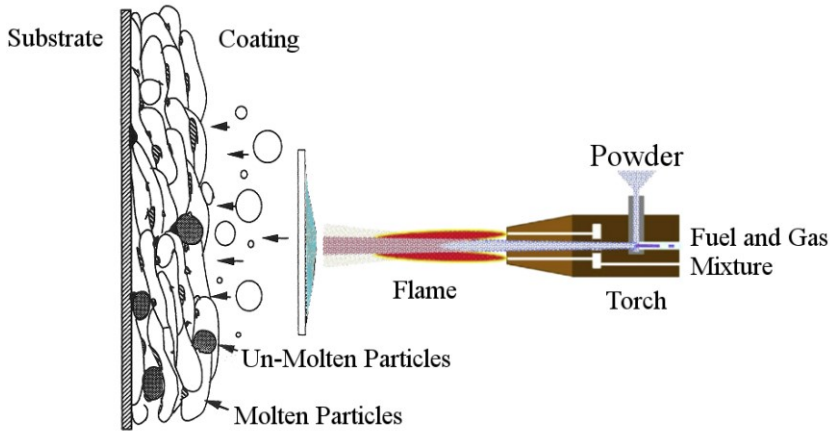

Figure 3: Schematic of flame spraying process [33]

The use of thermal spray processes may provide an alternative method to fabricate heating elements for FRPC wind turbine blades that are exposed to cold climates, different to the embed wire and plate resistive heating elements that have been previously used. Various studies have proposed the use of thermal spray processes in the fabrication of heating elements (or resistive heaters) [36, 38]. For example, Lamarre, *et al*. [36] have assessed and modeled the performance of FeCrAl wire-fed flame-sprayed coatings as heating elements on titanium substrates, obtaining temperatures above 450°C when 5 W/cm^2 of power was applied. However, the application of thermal spray processes to fabricate coatings on FRPC structures has only been recently initiated. Some investigators have deposited aluminum alloy coatings by flame spraying on to FRPC plates that have been used in structural health monitoring systems [35]. Robitaille, *et al*. [39] have deposited zinc coatings by pulsed-gas dynamic spraying on carbon/epoxy composites that were designed for use in aircraft structures to provide surface protection of the substrate. Given that the heat source of the thermal spray process is close to or in direct contact with the substrate, burning and degradation would be likely to occur in fiber-

reinforced polymer composite substrates at temperatures above 450^{o}C [39, 40]. Previous studies have shown that it is possible to deposit aluminium-12 wt.% silicon (Al-12Si), with a melting point of 577°C [40, 41], on FRPCs, without significant damage to the underlying substrate. However, no studies have focused on the deposition of high melting point alloys such as nickel-20 wt% chromium (Ni-20Cr) and nickel-chromium-aluminum-yttrium (NiCrAlY), with melting points on the order of 1400°C [42, 43], on FRPCs by using the flame spray process. High melting point alloys such as Ni-Cr based alloys are used in industry to fabricate heating elements in various devices and applications [44–46].

1.5. OBJECTIVES

The overall objectives of this study were to:

1. Develop a methodology to produce heating elements for FRPC based on flame-sprayed NiCr and NiCrAlY coatings, without burning or degrading the FRPC substrate.
2. Validate the performance of the coatings by:
    a. Testing them as heating elements under free- and forced- convective conditions at different ambient temperatures
    b. Exposing the samples to icing conditions and testing the performance of the coating as de-icing systems.
3. Develop a finite length-scale one-dimensional, transient, heat conduction model with phase change that estimates the de-icing process of the spray-coated FRPC plates.
4. Validate the heat conduction model with experimental data.

1.6. THESIS ORGANIZATION

This thesis is divided into several chapters. Following the Introduction in Chapter 1, Chapter 2 describes the experimental method used to fabricate and test the heating elements. Chapter 3 describes the mathematical model developed to describe the de-icing process. Chapter 4 presents the results and analysis of the tests and mathematical model. Chapter 5 presents the conclusions of this study, and Chapter 6 proposes future work that may be extended from this thesis study.

2. EXPERIMENTAL METHOD

This experimental method describes the process used to manufacture the samples used in this study, the characterization of the coating-substrate system, and the assessment of the performance of the coatings as heating elements.

2.1. SUBSTRATE PREPARATION

A $[0°_{20}]$ ply fiber-reinforced polymer composite (FRPC) plate was fabricated by aligning and stacking unidirectional fiber-reinforced epoxy prepreg plies (E-Glass Cycom 1003, Cytec Engineered Materials, Woodland Park, NJ, USA) over a glass plate. In order to consolidate the prepreg plies and promote the adhesion between them during the curing process, a 510 mm x 510 mm x 6 mm thick glass plate was placed on top of the composite stack. The 2.5 kg weight of the plate generated a 0.5 kPa pressure on the prepregs. The resin was cured at a controlled temperature of 166°C in an oven (Fisher Senior Forced Draft Isotemp Oven, Fisher & Paykel Appliances, Mississauga, ON, Canada) for one hour. Figure 4 shows a FRPC plate after curing. Samples with dimensions of 20 mm x 130 mm were cut from the resulting plate. The samples were carefully cleaned with acetone and dried in air. Two copper strips that were 1.5 mm thick were attached with high-strength epoxy adhesive (Scotch-Weld DP460 Off-White, 3M, St. Paul, MN, USA) at opposite ends on one of the surfaces of the polymer-based composite samples. The distance between the strips was 120 mm. The copper strips served as electrical terminals in the heating element circuit. Figure 5 shows a picture of a typical FRPC plate, with the copper strip terminals, that was used in this study.

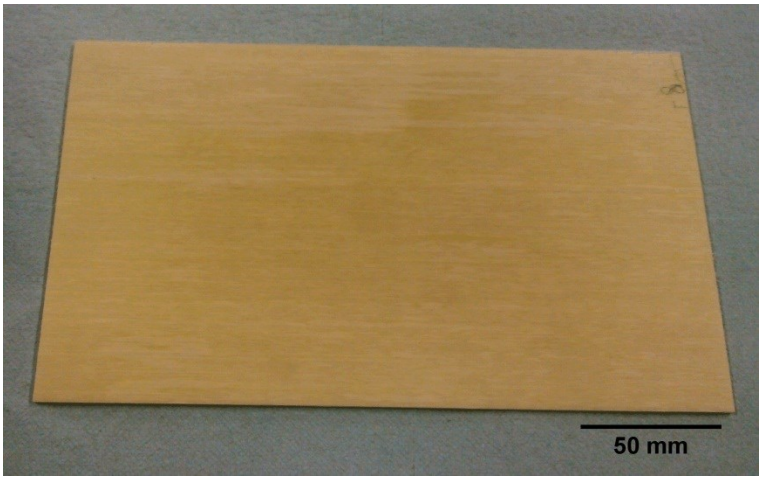

Figure 4: FRPC ply after curing process

A layer of high-strength epoxy adhesive (Scotch-Weld DP460 Off-White, 3M, St. Paul, MN, USA) and #220 grit garnet sand was manually applied in order to promote the adhesion of the coating by increasing the roughness of the surface. Previous research work [35, 40] have shown that the sand-resin layer highly increases the adhesion of the coating on the surface of the FRPC plates and eliminates the need for grit blasting, which would cause damage to the polymer-based substrate [35, 40, 41]. The sand-resin layer was cured at room temperature for more than 8 hours as suggested by the manufacturer. Prior to the application of the coatings, the copper strip terminals were grit-blasted with #24 alumina grit (Manus Abrasive Systems, Inc., Edmonton, AB, Canada) to promote adhesion of the coating on to the strips. Given that the grit-blasting process has been found to damage the polymer-based composite [41], thermal spray masking tape (170-10S Red, Green Belting Industries, Mississauga, ON, Canada) was used to protect the composite during the grit-blasting process of the copper.

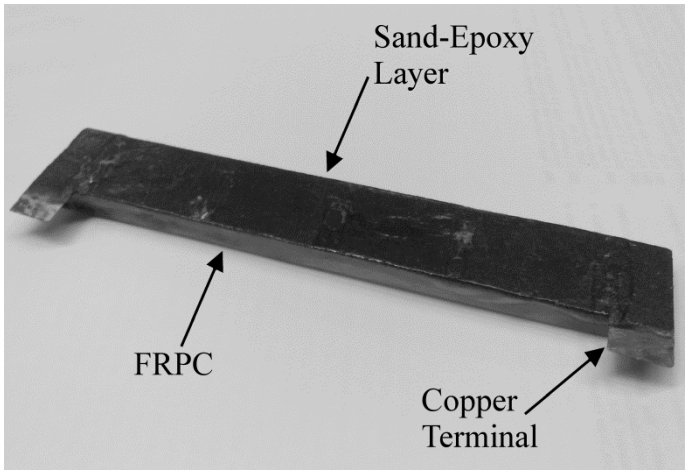

Figure 5: Typical FRPC plate with copper terminals and sand-epoxy layer

2.2. COATING DEPOSITION

An oxy-acetylene flame spray torch (6P-II, Oerlikon Metco, Westbury, NY, USA) was used to deposit nickel-20% wt. chromium, hereafter referred to as NiCr (METCO 43F-NS, Oerlikon Metco, Westbury, NY, USA), and nickel-chromium-aluminum-yttrium, hereafter referred to as NiCrAlY (Amdry 962, Oerlikon Metco, Westbury, NY, USA). The size of the NiCr powder particles (76.3 wt.% Ni, 19.5 wt.% Cr, 1.2 wt.% Si, 1.0 wt.% Fe, 1.5 wt.% Mn, others 0.5 wt.%) varied from 45 μm to 106 μm (-106+45 μm). The size of the NiCrAlY powder particles (65 wt.% Ni, 23 wt.% Cr, 11 wt.% Al, 1 wt.% Y) varied from 53 μm to 106 μm (-106+53 μm). A volumetric powder feeder (5MPE, Oerlikon Metco, Westbury, NY, USA), using argon as the carrier gas, was used to transport the powder to the torch. The argon pressure was set to achieve a volumetric flow rate of 0.56 m^3/h (20 standard cubic feet per hour) in order to produce a flow meter reading (FMR) for the NiCr and NiCrAlY powders. A combustion flame

was generated in the torch by mixing acetylene and oxygen at specific rates for each powder. Table 1 shows the spray parameters that were used for depositing the powders.

Table 1: Spray parameters for NiCr and NiCrAlY coating

Parameter	NiCr	NiCrAlY
Acetylene Flow [m^3/h]	0.9	0.9
Oxygen Flow [m^3/h]	2.1	1.5
Argon Pressure (Carrier Gas) [kPa]	414	552
Powder Flow Rate (FMR)	120	150
Robot Speed [mm/s]	500	500
SOD [mm]	229	254

In order to ensure consistent and repeatable deposition of the coating, the flame spray torch was controlled by a robot (HP-20, Motoman Yaskawa Electric Corp., Waukegan, IL, USA). The substrate was held stationary while the torch was moved linearly at 500 mm/s at a constant stand-off distance (SOD) from the substrate. Figure 6 shows the equipment that was used in the deposition of the coatings. Table 1 lists the SOD for the deposition of each powder. The distance that the robot traversed up between depositions of a single line of coating was set to 5 mm. The torch made two (2) and three (3) passes to obtain continuity in the NiCrAlY and NiCr coating, respectively. Two substrate samples were sprayed with each powder.

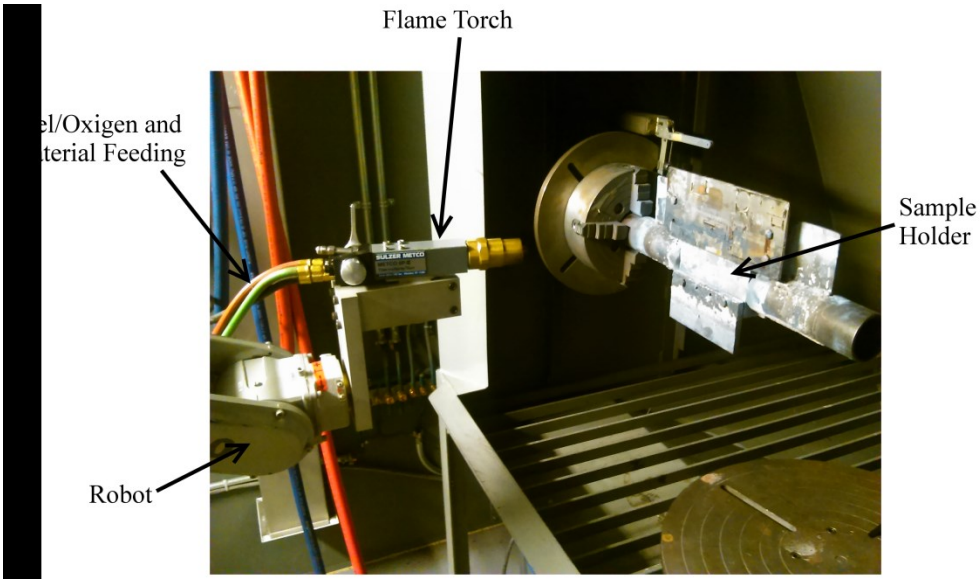

Figure 6: Equipment used in the deposition of the coatings

2.3. COATING AND SUBSTRATE CHARACTERIZATION

Samples of the coated plates were sectioned and cold-mounted in an epoxy resin (LECO, Mississauga, ON, Canada) for microstructural analysis. Two sections of coated plate samples were cold-mounted for each powder material. Each cold-mounted coating was ground using 180, 400, 800, and 1200 grit paper (LECO, Mississauga, ON, Canada), and polishing was conducted with a 3 μm diamond slurry (LECO, Mississauga, ON, Canada) as final step. Two samples were mounted, ground, and polished for each coating material type. A scanning electron microscope (SEM) (EVO MA 15, Zeiss, Cambridge, UK) equipped with energy-dispersive X-ray spectroscopy (EDX) was used to analyze the cross-sectional microstructure of the coatings and to determine the chemical composition of the coatings. Images of the cross-section were captured using the backscattering electron (BSE) mode. A sputter coater (EM SCD 005, Leica-Baltec Instrument, Balzers, Liechtenstein) with a carbon evaporation accessory was

used to deposit a thin carbon coating onto the cold-mounted samples to prevent sample charging in the SEM. An image analysis software (ImagePro, Media Cybernetics, Bethesda, MD, USA), coupled with the SEM micrographs, was used to estimate the thickness and porosity of the coatings. At least 5 images of each sample (n = 5) were used to determine the average thickness and the average porosity of the coatings. The porosity of the coatings was determined by using the particle analysis tool of the image analysis software. The images were thresholded to have the porous as only element in the image. Finally, particles with circularity between 0.5 and 1 were measured by the image analysis software.

The fiber volume fraction (σ_r) of the composite was determined in accordance with ASTM Standard D2584 [47]. The mass of two 25.4 mm x 25.4 mm specimens was measured prior to and after placing them inside an oven (Fisher Senior Forced Draft Isotemp Oven, Fisher & Paykel Appliances, Mississauga, ON, Canada) at a temperature of 560°C for 4 hours. This process completely degraded and removed the polymeric phase of the composite from the sample, leaving only the glass fiber reinforcement. The fiber volume fraction of each sample was calculated by using the following formula shown in Eq. 1 [48]:

$$\sigma_r = \frac{\frac{m_r}{\rho_r}}{\frac{m_r}{\rho_r} + \frac{m_m}{\rho_m}}, \quad (1)$$

where m is the mass, ρ is the density, and the subscripts r and m represent the fiber and matrix, respectively.

The fiber volume fraction can be used in the rule of mixtures to predict the thermal properties of the composite samples. The rule of mixtures, Eq. 2, gives an estimated value for any property, k_c, as the weighted average of the bulk properties of the fiber and matrix [48, 49] as

$$k_C = \sigma_r k_r + (1 - \sigma_r) k_m, \tag{2}$$

where k_r and k_m are the bulk properties of the fiber and matrix, respectively.

The thermal conductivity in the longitudinal and transverse directions of the fibers in the FRPC were measured by using a thermal properties analyzer (TPS 2500, Thermtest Hot Disk, Gothenburg, Sweden), equipped with a controlled temperature chamber. The measurements were taken at -25°C, -5°C, 25°C, and 50°C temperature set-points. The samples were placed into the chamber at each set temperature and held for 20 minutes in order to reach thermal equilibrium with the environment. Afterwards, a Kapton-insulated actuator/sensor, in direct contact with the surface of the specimen, heated the sample surface to within about 1°C of the set-point temperature and measured the rate of change of the temperature in the sample. Analysis software that comes complete with the thermal properties analyzer was used to calculate the thermal conductivity and diffusivity based on the temperature measurements and rate of change of temperature in the sample as the sensor heated its surface. A total of 15 measurements over two samples at each ambient temperature were collected.

2.4. ELECTRICAL CHARACTERIZATION

The electrical resistance of the coatings was determined at -25°C, -5°C, 25°C, 50°C and 80°C ambient temperatures. A controlled thermal bath (TPS 2500, Thermtest Hot Disk, Gothenburg, Sweden), equipped with an insulated sample chamber, was used to control the temperature of the coating and composite specimens. The samples were held in the chamber for 20 minutes to allow for thermal equilibrium between the samples and the environment. Through the copper strips that were attached to the coated composite samples, electrical current over 3 V, 4.5 V, 6 V, 7.5 V, 9 V, 12 V, and 15 V was supplied with a power supply (1692 DC, B&K Precision Corporation, Yorba Linda, CA, USA). The electrical current (I) was measured three times with a multimeter and the average was determined. Curves of voltage (V) versus current (I) were prepared. The linearity of the curves was verified by plotting straight lines to fit the experimental data of voltage and current and calculating the constant of proportionality and correlation of the fitted curves. Three measurements were performed for each voltage using two coated FRPC samples for each material (NiCr and NiCrAlY).

2.5. JOULE HEATING TESTS

The performance of the coatings as Joule heating elements was tested. The power supply was used to provide electrical current thought the copper terminals over 3 V, 4.5 V, and 6 V. K-type thermocouples (Omega, Montréal, QC, Canada) were attached to the coated and bare surfaces of the composite sample using an instant adhesive (Black Max 3GM, Düsseldorf, Germany). There were 5 thermocouples on each side of the sample, each spaced 30 mm apart. The ambient temperature was measured by using a J-type thermocouple (Omega, Montréal, QC,

Canada). The transient temperature measurements were collected with a data acquisition system (SCXI-1600, National Instruments, Austin, TX, USA) at a rate of 10 Hz (10 data points per second). Figure 7 shows a diagram of the experimental assembly for the Joule heating tests.

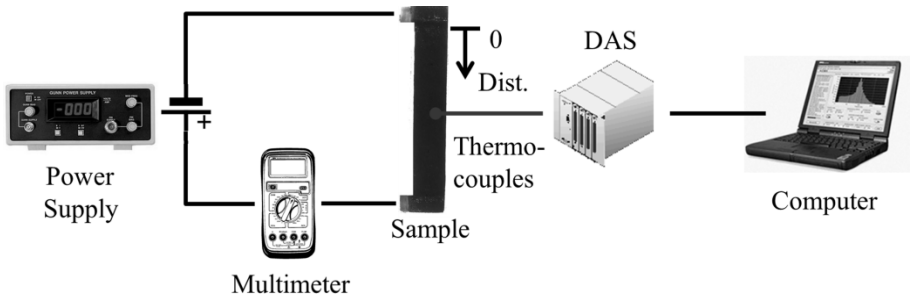

Figure 7: Experimental assembly for electrical characterization and Joule heating tests

The tests were performed in an 18 m^3 cold room (Foster Refrigerator USA, Kinderhook, NY, USA) that was equipped with a temperature controller. The tests were conducted at an ambient temperature of -25°C and -5°C (± 3°C) with the cold room in operation and at 23°C (± 3°C) without operation of the cold room. The samples were placed in a 2 m x 0.66 m x 0.48 m closed duct, as shown in Fig. 8, to reduce the effects of circulating air currents inside the cold room. Forced convection conditions were simulated by using a 0.25 kW (0.33 hp) direct-drive axial fan (DDA-12-10033B, Leader Fan Industries, Toronto, ON, Canada). A rectangular orifice in the duct allowed access to the samples. A digital manometer (475-1-FM, Dwyer Instruments, Michigan City, IN, USA) was used to measure the air speed after exit from the fan and within the vicinity of the specimen. The Joule heating tests were performed three times on each coated FRPC sample at each ambient temperature.

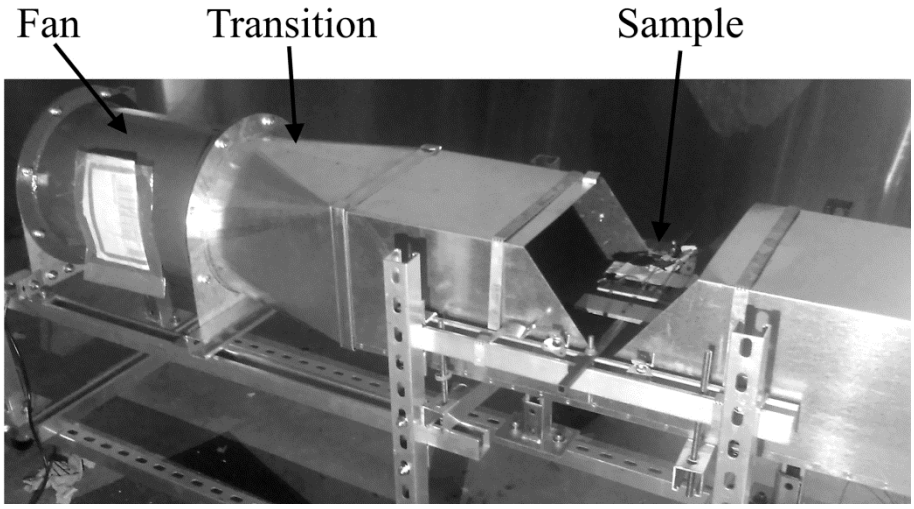

Figure 8: Experimental air duct assembly

2.6. DE-ICING TESTS

The performance of the coatings as heating elements for de-icing purposes was tested. The samples were placed inside the closed duct as shown in Fig. 8. A K-type thermocouple (Omega, Montréal, QC, Canada) was attached to both the surface of the coating and the uncoated FRPC sample surface. A water spray nozzle (¼" MJB8MX, John Brooks Company Ltd, Edmonton, AB, Canada), which was attached to the top of the duct, was used to dispense water droplets at a rate of 2 L/min over the sample inside the duct. The nozzle was placed between the sample and the 0.25 kW (0.33 hp) direct-drive axial fan that was used to simulate forced convection conditions over the sample, as shown in the schematic of Fig. 9. The nozzle was attached to a pump (Series 5800, Aquatec Water Systems Inc., Irvine, CA, United States) with a 6.4 mm (0.25 in) diameter water hose. The size of the droplets was expected to be between 500 μm and 1000 μm, as specified by the manufacturer of the nozzle [50]. This size of the droplets simulated that of light to moderate rain, which leads to the formation of glaze ice or

freezing rain [10, 14]. Glaze ice or freezing rain occur when a drop of cold water (at as low as -30°C) impacts a surface below 0°C and does not completely freeze upon impact, but moves on the surface as the freezing process occurs. The resulting ice from this phenomenon has high density and strong adhesion to the surface [10, 14].

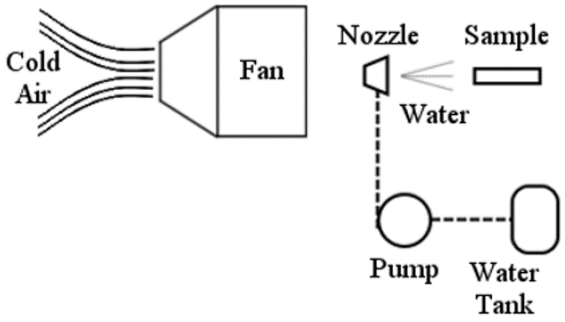

Figure 9: Schematic of the water dispensing system

The tests were performed inside the cold room at ambient temperatures of -25°C, -15°C, and -5°C (± 3°C). The ambient temperature was measured by using a J-type thermocouple (Omega, Montréal, QC, Canada). Once the cold room achieved the set ambient temperature, water was sprayed through the nozzle for 5 minutes to permit the formation of a layer of ice over the sample. The ice was allowed to equilibrate with the environment, after which the thickness of the layer of ice was measured at 5 different locations along the length of the sample. A K-type thermocouple (Omega, Montréal, QC, Canada) was attached to the layer of ice by placing it on top of the ice and depositing droplets of cold water over it. A power supply (1692 DC, B&K Precision Corporation, Yorba Linda, CA, USA) was used to provide electric

current though the copper terminals over 4.5 V, 6 V, and 7.5 V. The transient temperature measurements were collected with a data acquisition system (SCXI-1600, National Instruments, Austin, TX, USA) at a rate of 10 Hz (10 data points per second). Figure 7 shows a flow diagram of the test assembly that comprised the samples and the power supply as well as the thermocouples connected to the data acquisition system.

The experimental method described in this section was used in the fabrication of the samples used in this study. In addition, a description of the microstructural, thermal, and electrical characterization of the coating-substrate system was provided. Finally, the performance of the coatings as heating elements for wind turbines was assessed in heating and de-icing tests under different ambient conditions.

3. MATHEMATICAL MODEL

The mathematical model in this thesis aims to examine the heat conduction during the de-icing process on FRPC plates that are heated by metallic coatings through Joule heating. A finite length-scale one-dimensional, transient, heat conduction model with phase change was developed to estimate the de-icing time of the FRPC plates at different ambient temperatures under forced convection conditions. Experimental data was used to validate the analytical models.

The de-icing process to melt an ice layer with thickness, δ, that is at an initial temperature, T_i, and under ambient temperature, T_∞, by effect of the heat generated in the coating, can be divided into two stages. Initially, the heat generated by the coating increases the temperature of the ice from the initial temperature to the melting temperature, T_f. Isothermal melting of the ice follows afterwards. At constant temperature, T_f, a melting front (or liquid-solid interface) moves from the surface of the coating towards the free surface of the ice. The following sub-sections elaborate on the modeling of the heating and melting stages of the de-icing process.

3.1. HEATING ICE

Heating ice from an initial temperature, T_i, to its melting point, T_f, can be determined by considering a lumped-capacity model (or lumped capacitance model). This model is a simple

approach to solving transient heat transfer problems [51, 52]. The lumped-capacity method assumes that the temperature in a body does not vary spatially. This approximation is valid for situations where the Biot number, $\mathrm{Bi} = \frac{h\delta}{k_s}$, is lower than 0.1 [31]. In this study, the thickness of the ice, δ, is lower than 5 mm and its thermal conductivity, k_s, is low and on the order of 2.2 W/m-K [53]. Depending on the value of the heat transfer coefficient (h), a Biot number lower than 0.1 may occur, indicating negligible temperature variation across the cross section of the ice [51, 52].

The temperature distribution within a body, in this case a layer of ice as shown in Fig. 10, is determined by considering the law of conservation of energy. Without energy generation, the law is

$$\dot{E}_{\mathrm{in}} - \dot{E}_{\mathrm{o}} = \Delta\dot{E}, \tag{3}$$

where the rate of energy into the ice is

$$\dot{E}_{\mathrm{in}} = q''_{\mathrm{g}} A - hA(T_{\mathrm{F}} - T_{\infty}) = \frac{V^2}{R} - hA(T_{\mathrm{F}} - T_{\infty}). \tag{4}$$

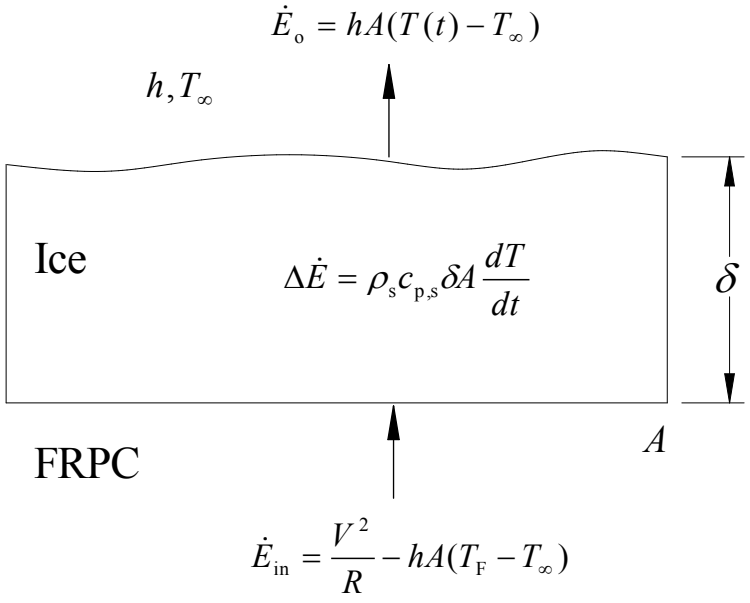

Figure 10: Energy balance of ice control volume

The energy generated in the coating by means of Joule heating (q''_g) can be expressed as a function of the applied voltage, V and the electrical resistance of the coating, R. It was assumed that the coating is Ohmic and that the efficiency of energy generation through Joule heating by the coating is 1. The $hA(T_F - T_\infty)$ term is the heat that is lost by convection, as described by Newton's law of cooling, from the FRPC plate surface at temperature, T_F, to the environment at a temperature, T_∞. The temperature in the FRPC plate surface was assumed to be constant, and was taken as the average surface temperature. The convective heat loss serves to reduce the total energy generated in the coating, with the remainder transferred to the ice.

Energy was removed from the ice at its free surface by way of convection. That energy loss is defined as

$$\dot{E}_{\mathrm{o}} = hA\left[T(t) - T_{\infty}\right]. \tag{5}$$

In addition to convection, the energy in the layer of ice on the FRPC sample was removed by way of radiation. However, radiation heat transfer mode is not considered in the formulation of this model given that the heat transfer by way of radiation is expected to be low compared with that via convective heat transfer. The radiation heat transfer from the layer of ice at temperature, T, to the cold room at temperature, T_{∞}, is equal to $\dot{E}_{\mathrm{R}} = \ell \varpi A\left[T^4(t) - T^4{}_{\infty}\right]$, as described by Stefan-Boltzmann law for radiative heat transfer, where, ϖ is the Stefan-Boltzmann constant, equal to 5.6703x10-8 W/m^{2}K^4, and ℓ the emissivity of ice, equal to 0.96 [54]. The resultant heat loss by means of radiation is expected to be significantly lower than the convective heat loss. For instance, the radiative energy loss from a layer of ice at melting point of 0°C (273.15 K) inside a cold room at temperature of -10°C (263.15 K), would be 0.1 W/m^2. Due to the low temperature difference between the ice and the room, and the high convective heat transfer coefficient, as consequence of the air flow from the fan (Fig. 8), the radiation heat loss is expected to be approximately one order of magnitude lower than the convective heat loss. This assumption will be confirmed in further discussion with regards to the convective heat transfer coefficient.

The resulting change in energy in the ice is given as

$$\Delta\dot{E} = \rho_{\mathrm{s}} c_{\mathrm{p,s}} \delta A \frac{dT}{dt}, \tag{6}$$

where the δA term is the volume of the ice layer, ρ_s is the density, and $c_{p,s}$ is the heat capacity of the ice. Substituting Eqs.4 - 6 into Eq. 3 gives

$$\frac{V^2}{RA} - h\left[T(t) + T_F - 2T_\infty\right] = \rho_s c_{p,s} \delta \frac{dT}{dt}. \tag{7}$$

Equation 7 is solved by direct integration with the initial condition, $T(t=0) = T_i$, to give

$$T(t) = \left(T_i + T_F - 2T_\infty - \frac{V^2}{RAh}\right)\exp\left(\frac{-ht}{\rho_s c_{p,s} \delta}\right) - T_F + 2T_\infty + \frac{V^2}{RAh}. \tag{8}$$

Equation 8 can be used to predict the heating time of ice from an initial temperature, T_i, to the fusion temperature, T_f. The constants and general properties of solid ice are summarized in Table 2.

Table 2: Properties for solid water in Eq. 8 [53]

Property, symbol	**Value**
Specific heat capacity, $c_{p,s}$	2010 J/kg-K
Density, ρ_s	917 kg/m^3
Thermal conductivity, k_s	2.2 W/m-K

3.2. MELTING OF ICE OF FINITE THICKNESS

A one-dimensional transient heat conduction model, in rectangular co-ordinates, was developed to estimate the melting time of the ice layer on the coating. Figure 11 shows a schematic of the model used in this analysis. Once at the melting temperature, a liquid-solid interface, $x_i(t)$, moves outward from the coating-ice interface to the free surface of the ice. The melting of the ice is complete when the liquid-solid interface arrives at the free surface of the ice.

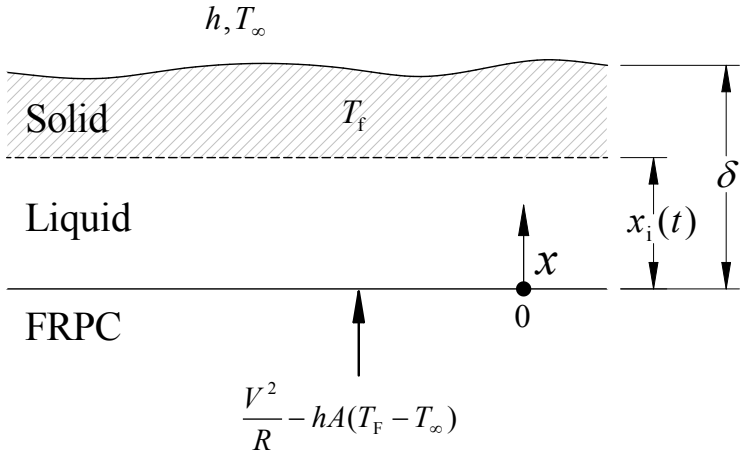

Figure 11: Schematic of melting of a layer of ice

The governing equations of the temperature distribution in the solid and liquid phases are

$$\frac{d^2T_L}{dx^2} = \frac{1}{\alpha_L}\frac{dT_L}{dt}, \qquad 0 \le x < x_i(t), \tag{9}$$

$$T_s = T_f, \qquad x_i(t) < x \le \delta. \tag{10}$$

The boundary and initial conditions are

$$-k_{\mathrm{L}}\frac{dT_{\mathrm{L}}(0,t)}{dx}=\frac{V^2}{RA}-h(T_{\mathrm{F}}-T_{\infty}), \tag{11}$$

$$T_{\mathrm{L}}(x_{\mathrm{i}},t)=T_{\mathrm{f}}, \tag{12}$$

$$T_{\mathrm{L}}(x,0)=T_{\mathrm{f}}. \tag{13}$$

The interface energy equation, which describes conservation of energy at the liquid-solid interface, will be used to determine the transient liquid-solid interface location, $x_{\mathrm{i}}(t)$. The interface energy equation and initial condition are

$$-k_{\mathrm{L}}\frac{dT_{\mathrm{L}}(x_{\mathrm{i}},t)}{dx}=\rho_{\mathrm{L}}\hbar\frac{dx_{\mathrm{i}}}{dt}, \qquad t>0 \tag{14}$$

$$x_{\mathrm{i}}(0)=0. \tag{15}$$

Equations 9 - 15 describe a finite length-scale melting problem of a layer of ice with thickness, δ, which has been initially heated to the fusion temperature, T_{f}. Given the non-homogeneity of the boundary conditions of Eqs. 11 and 12 and the finite length-scale of the ice, the governing equation of the temperature distribution in the liquid phase (Eq. 9) was solved by using superposition and the separation of variables method. The superposition method assumes that the solution for $T_{\mathrm{L}}(x,t)$ is the sum of two functions, one, $\Psi(x,t)$ depending on x and t for the homogeneous solution of $T_{\mathrm{L}}(x,t)$, and a second, $\Phi(x)$ that depends on x, only and is the particular solution of $T_{\mathrm{L}}(x,t)$. This is,

$$T_{\mathrm{L}}(x,t) = \Psi(x,t) + \Phi(x). \tag{16}$$

Then, substituting Eq. 16 into Eq. 9 and separating,

$$\frac{d^2\Psi}{dx^2} = \frac{1}{\alpha_{\mathrm{L}}}\frac{d\Psi}{dt}, \tag{17}$$

$$\frac{d^2\Phi}{dx^2} = 0. \tag{18}$$

Equation 16 is substituted into the boundary and initial conditions of Eqs. 11 - 13, followed by separation, to yield two homogeneous boundary conditions and one non-homogeneous initial condition for Ψ in Eq. 17, and two non-homogeneous boundary conditions for Φ in Eq. 18.

The solution for $\Psi(x,t)$ in Eq. 17 was assumed to be the product of a function $\mathrm{X}(x)$, depending on x only, and $\Gamma(t)$, depending on t, only, so that

$$\Psi(x,t) = \mathrm{X}(x)\Gamma(t). \tag{19}$$

After substituting Eq. 19 into Eq. 17 and separating,

$$\frac{d^2\mathrm{X}_n}{dx^2} + \lambda_n^2\mathrm{X}_n = 0, \tag{20}$$

$$\frac{d\Gamma_n}{dt} + \alpha_{\mathrm{L}} \lambda_n^2 \Gamma_n = 0 . \tag{21}$$

Integration of Eqs. 20 and 21 gives

$$\mathrm{X}_n(x) = A_n \sin(\lambda_n x) + B_n \cos(\lambda_n x) , \tag{22}$$

$$\Gamma(t) = C_n \exp(-\alpha_{\mathrm{L}} \lambda_n{}^2 t) . \tag{23}$$

where A_{n}, B_{n}, and C_{n} are integration constants. Application of the boundary conditions at $x = 0$ (Eq. 11) for $-k_{\mathrm{L}} \dfrac{d\Psi(0,t)}{dx} = 0$ and at $x = x_{\mathrm{i}}(t)$ (Eq. 12) for $\Psi(x_{\mathrm{i}}, t) = 0$ to Eq. 22 gives

$$A_n = 0 , \tag{24}$$

$$\lambda_n = \left(\frac{2n-1}{2} \right) \frac{\pi}{x_{\mathrm{i}}} , \qquad n = 1, 2, 3\ldots \tag{25}$$

where Eq. 25 can be used to find the eigenvalues, λ_n. The solution for $\lambda_n = 0$ in Eqs. 20 and 21 will yield $\mathrm{X}_0(x)\Gamma_0(t) = 0$. Therefore, the solution for $\Psi(x,t)$ is

$$\Psi(x,t) = \sum_{n=1}^{\infty} a_n \cos(\lambda_n x) \exp(-\alpha_{\mathrm{L}} \lambda_n^2 t) , \tag{26}$$

where $a_n = B_n C_n$.

The particular solution, as solved from Eq. 18, is

$$\Phi(x) = Dx + E , \tag{27}$$

where D and E are integration constants. Application of the boundary conditions at $x = 0$ (Eq. 11) for $-k_{\mathrm{L}} \dfrac{d\Phi(0)}{dx} = \dfrac{V^2}{RA} - h(T_{\mathrm{F}} - T_{\infty})$ and at $x = x_{\mathrm{i}}(t)$ (Eq. 12) for $\Phi(x_{\mathrm{i}}) = T_{\mathrm{f}}$ to Eq. 27 gives

$$D = -\frac{1}{k_{\mathrm{L}}}\left[\frac{V^2}{RA} - h(T_{\mathrm{F}} - T_{\infty})\right] \text{ and} \tag{28}$$

$$E = T_{\mathrm{f}} + \frac{x_{\mathrm{i}}}{k_{\mathrm{L}}}\left[\frac{V^2}{RA} - h(T_{\mathrm{F}} - T_{\infty})\right]. \tag{29}$$

The temperature distribution in the liquid becomes

$$T_{\mathrm{L}}(x,t) = T_{\mathrm{f}} + \left[\frac{V^2}{RA} - h(T_{\mathrm{F}} - T_{\infty})\right]\frac{(x_{\mathrm{i}} - x)}{k_{\mathrm{L}}} + \sum_{n=1}^{\infty} a_n \cos(\lambda_n x)\exp(-\alpha_{\mathrm{L}}\lambda_n{}^2 t). \tag{30}$$

The integration constant, a_n, can be found by applying the initial condition of Eq. 13. Equation 9 is a Sturm-Liouville equation. Therefore, orthogonality can be applied over the region of $0 \le x < x_{\mathrm{i}}(t)$ in the determination of a_{n}. As follows, and after application of Eq. 13,

$$\left[\frac{V^2}{RAk_{\mathrm{L}}} - \frac{h(T_{\mathrm{F}} - T_{\infty})}{k_{\mathrm{L}}}\right]\int_0^{x_{\mathrm{i}}(t)} (x_{\mathrm{i}} - x)\cos(\lambda_n x)dx + a_n \int_0^{x_{\mathrm{i}}(t)} \cos^2(\lambda_n x)dx = 0. \tag{31}$$

The constant, a_n is

$$a_n = \frac{8x_{\mathrm{i}}}{(2n-1)^2\pi^2}\left(\frac{V^2}{RAk_{\mathrm{L}}} - \frac{h(T_{\mathrm{F}} - T_{\infty})}{k_{\mathrm{L}}}\right). \tag{32}$$

The transient liquid-solid interface location, $x_i(t)$, is an unknown variable in the temperature distribution function of Eq. 30. The interface energy equation of Eq. 14 is solved with the initial condition of Eq. 15 to find the liquid-solid interface location. Knowledge of the liquid-solid interface location during the de-icing process will allow for estimation of the melting time of the ice. Differentiating Eq. 39, substituting it into Eq. 14, and solving gives

$$1-\sum_{n=1}^{\infty}\frac{4\sin\left(\frac{(2n-1)\pi}{2}\right)}{(2n-1)\pi}\exp\left(\frac{-\alpha_L(2n-1)^2\pi^2 t}{x_i^2}\right)=\left(\frac{h(T_F-T_\infty)}{k_L}-\frac{V^2}{RAk_L}\right)^{-1}\frac{\rho_L\hbar}{k_L}\frac{dx_i}{dt}. \quad (33)$$

A MATLAB (MathWorks, Inc., Natick, MA, USA) Runge-Kutta method differential equation solver, ode45, was used to solve the implicit expression for x_i in Eq. 33. Terms in the infinite series were added until the solutions converged to within 1% of the sum.

The transient liquid-solid interface location during the de-icing process can alternatively be predicted by considering the melting of a semi-infinite solid body initially at the melting temperature, T_f. The assumption of a semi-infinite extent of the solid phase during a melting problem is valid when the thickness of the liquid phase is small in comparison to the thickness of the solid phase. The assumption is no longer valid when the thicknesses of the liquid and solid phases are on the same order of magnitude. Stefan's solution, as detailed by Jiji [51] and Carslaw and Jaeger [55] shows that the transient liquid-solid interface location is expressed as

$$x_i(t)=\lambda\sqrt{4\alpha_L t}, \quad (34)$$

where λ is a constant given by the expression,

$$\lambda \exp(\lambda^2) = \frac{\sqrt{t_h}}{2\rho_L \hbar \sqrt{\alpha_L}} \left(\frac{V^2}{RA} - h(T_F - T_\infty) \right) \tag{35}$$

and t_h is the time required to heat the ice.

The mathematical model in this section aimed to predict the heating and melting times during the de-icing process on FRPC plates that are heated by metallic coatings through Joule heating. The de-icing process of a layer of ice over the FRPC samples was studied in two different stages: (1) a heating process in which the temperature of the ice increased from an initial temperature, T_i, to the fusion point, T_f, and (2) a second stage where the isothermal melting of the ice occurred. Experimental results were used to validate the models.

4. RESULTS AND DISCUSSION

4.1. COATING CHARACTERIZATION

Low magnification images were captured with SEM and were used to characterize the coating-FPRC substrate ensemble samples. Figure 12a shows a representative low magnification SEM image of a NiCr coating sample. The samples are composed of a 5.9 mm ± 0.2 mm (n = 15) thick FRPC substrate, a 215 μm ± 15 μm (n = 15) thick garnet sand-epoxy layer, and the NiCr coating with a thickness of 100 μm ± 15 μm (n = 20). The coating appears to be attached to the rough sand-epoxy layer and covers the substrate over its entire surface. The porosity was measured from high magnification SEM images (see Fig. 12b). It was found that the porosity of the coating was 6.8 vol.% ± 1.5 vol.% (n = 5) for NiCr. The high magnification images were also used to characterize salient features of the coatings. Three main splat morphologies were observed. (1) Those that were completely deformed and that were formed from molten particles during the spray deposition process, (2) round particles formed from partially deformed molten powder particles, and (3) un-molten powder particles formed by powder particles that evidence no change from the initial spherical shape of the powder. Inter-splat gaps, formed by the inability of the partially molten and un-molten particles to form contacts with other previously deposited particles, were also observed. The inter-splat gaps were the main source of porosity in the coating.

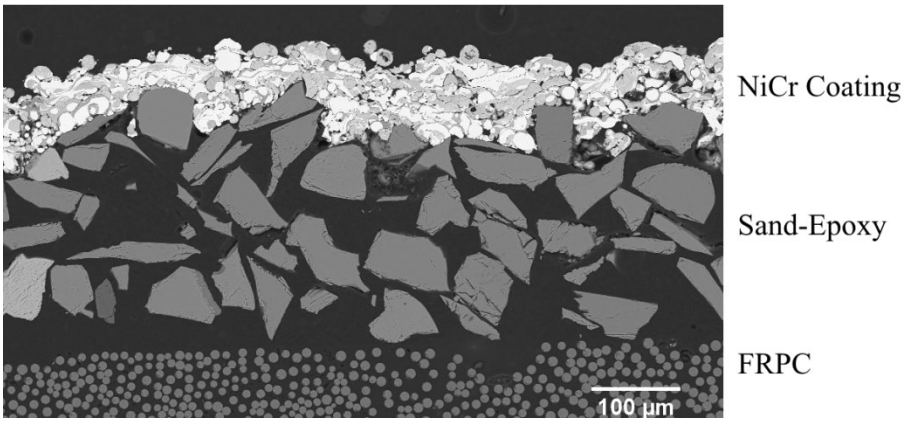

(a)

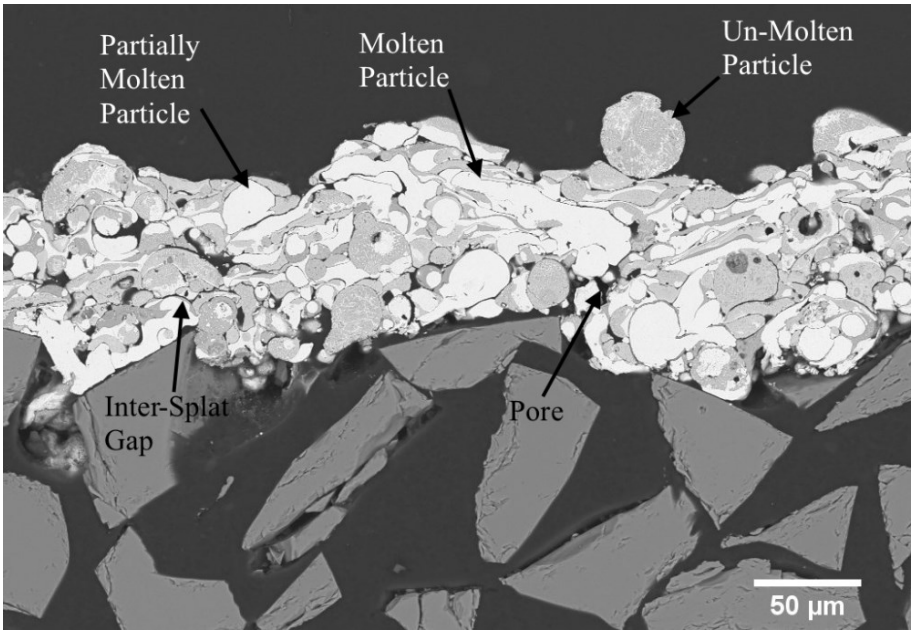

(b)

Figure 12: **a)** Low and **b)** high magnification SEM image of a NiCr coating

Figure 13a shows a low magnification SEM image of a NiCrAlY coating. The thickness of the coatings was found to be 80 μm ± 15 μm (n = 20). The NiCrAlY coating appears to be less homogeneous than the NiCr coating (see Fig. 12a), presenting voids across the substrate surface where the coating does not cover the composite and a varied thickness. The porosity was measured from high magnification SEM images (see Fig. 13b), and it was found that the porosity within the NiCrAlY coating was 1.7 vol.% ± 0.6 vol.% (n = 5). The same three types of splat morphologies that were observed for the NiCr coating were observed in the NiCrAlY coating. Inter-splat gaps were also observed. Energy-dispersive X-ray spectroscopy (EDX) was used in the characterization of the coatings. The composition of the coatings was confirmed to be nearly as that specified by the manufacturer. However, there was a noticeable content of oxygen in the coating. The oxygen found in the coatings suggests that oxidation occurred in the particles during the deposition process due to the high temperature and oxygen content in the flame. The temperature of the flame in the oxy-acetylene torch was found by Nelson, *et al*. [56] to be approximately 3400 K, where excess oxygen was used to generate the combustion flame.

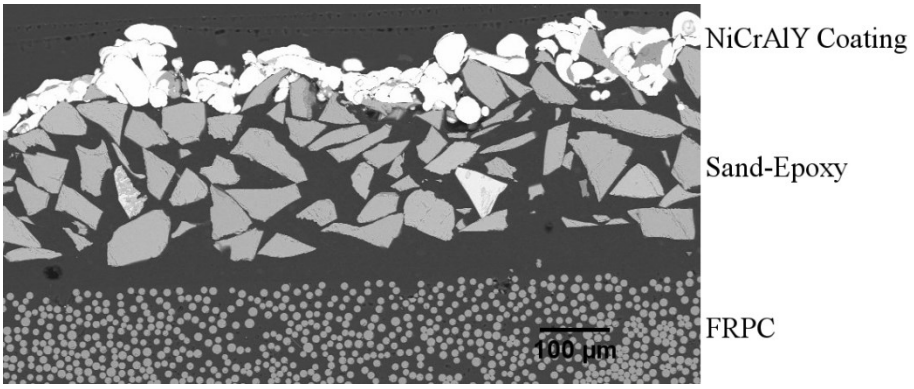

(a)

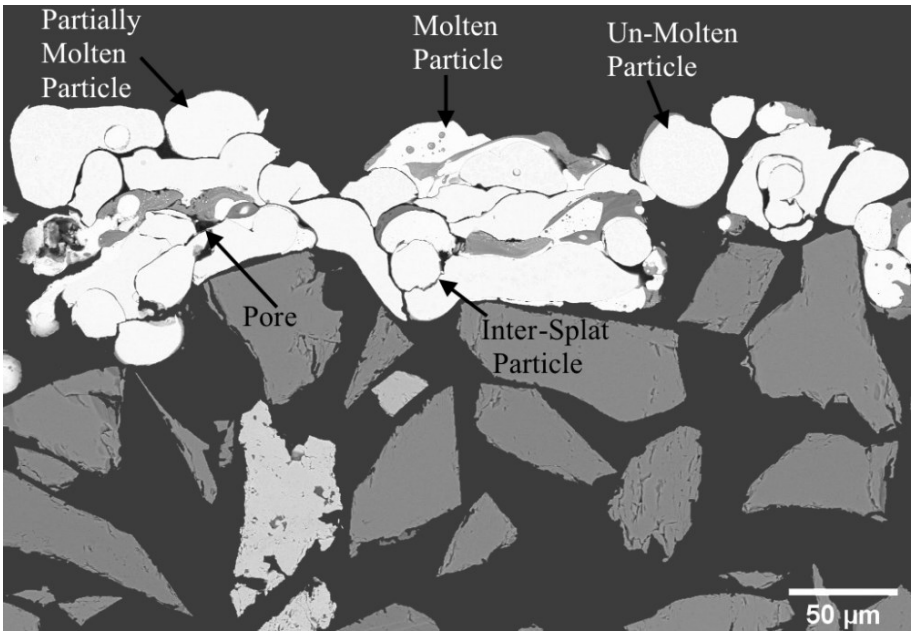

(b)

Figure 13: **a)** Low and **b)** high magnification SEM image of a NiCrAlY coating

4.2. SUBSTRATE CHARACTERIZATION

ASTM Standard D2584 was used to determine the fiber volume fraction in the composite substrate. From Eq. 1 [48], it was found that the fiber volume fraction of the specimens was 41 vol.% ± 0.2 vol.% (n = 2). This value of fiber volume fraction is characteristic of prepreg plies that were fabricated under low applied external pressure or vacuum conditions [35]. The values of the densities of the resin matrix and the fibers were taken as 1200 kg/m^3 and 2600 kg/m^3, respectively [40, 48]. The result of fiber volume fraction that is reported in this study is consistent with values previously reported for the glass-fiber reinforced composite that was used [40, 48].

The thermal conductivity (k) of the FRPC substrate was measured in the longitudinal and transverse direction at different temperatures. Figure 14 shows curves of the thermal conductivities of the FRPC as a function of temperature. Within the temperature range used in the measurements, the longitudinal thermal conductivity was found to decrease by about 10% from 0.48 W/m°C at -25 °C to 0.43 W/m°C at 50°C. On the other hand, the transverse thermal conductivity increased by 32%, from 0.27 W/m°C at -25°C to 0.36 W/m°C at 50°C. A simple linear regression was used to model the relationship between thermal conductivity and temperature by fitting the experimental results to a line. The slope of this line, usually termed a regression coefficient, provides information about the dependency of the dependent variable on the independent variable. In this case, the slope of the fitting line was lower than 0.005 W/m°C^2. This suggests that the thermal conductivity of the FRPC was weakly dependent on temperature [57]. The rule of mixtures of Eq. 2 can be applied to estimate the weighted average thermal

conductivity of the FRPC. From the work of other investigators [48], k_m and k_r were found to be approximately 0.2 W/m°C and 1 W/m°C, respectively at approximately 25°C. Then, the weighted average thermal conductivity of the FRPC substrate was approximately 0.53 W/m°C. This value is on the same order of magnitude as those of the transverse and longitudinal thermal conductivities that was measured in this study and shown in Fig. 14. The rule of mixtures assumes that the matrix and fibers are in perfect contact and are isotropic materials, that the diameter and space between fibers is uniform, and that the composite is free of voids [48]. However, the low-pressure curing process used in this work has been found to produce between 3 vol.% and 10 vol.% void content [58–60], which explains the difference observed between the values of thermal conductivity predicted by the rule of mixtures and those that were experimentally measured. The differences in transverse and longitudinal thermal conductivities shown in Fig. 14 indicate that the FPRC is anisotropic.

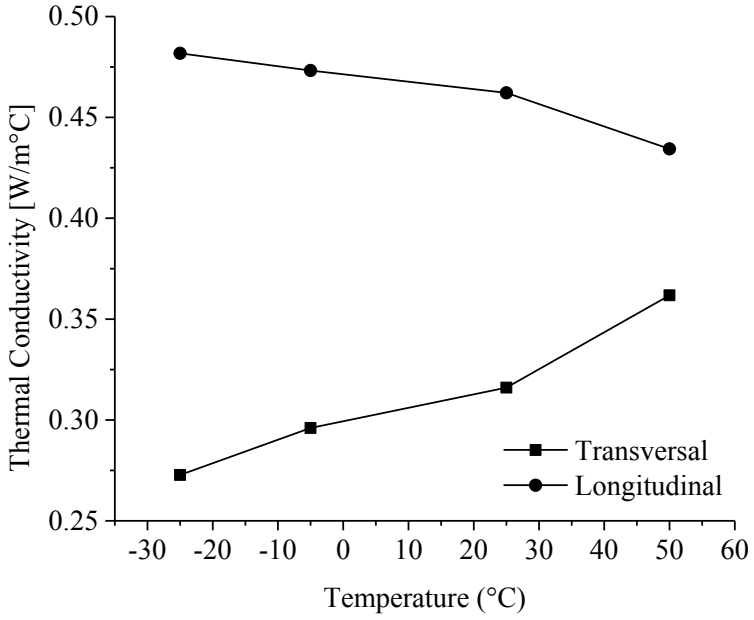

Figure 14: Longitudinal and transverse thermal conductivity of FRCP

4.3. ELECTRICAL CHARACTERIZATION

The magnitude of heat that is generated in a metal when electrical current is passed through it will depend on the electrical properties of the metal. In particular, the electrical resistivity of a material, which is an intrinsic property that quantifies the resistance to the flow of electrical current in a material, can be used to determine the quantity of heat is generated. As electrons with high initial energy flow through the metal, heat will be generated as the electrons experience resistance to their flow [61]. Values of electrical resistivity that are available from various standard sources are usually representative of bulk, isotropic materials. The coatings shown in Figs. 12 and 13 are porous and anisotropic, with a lamellar microstructure. As a result, the electrical properties that are tabulated in standard sources will not apply directly to the flame-sprayed coatings. Therefore, the electrical resistance of each coating was measured experimentally, and used to quantify the heat generated in the coatings when electrical current was passed through them. The electrical resistance (R) of the coatings was determined at different temperatures by using Ohm's law, $V = RI$. A material in which the relationship between voltage (V) and current (I) is linear is an Ohmic material and Ohm's law is valid. The value of the resistance and the validity of Ohm's Law may be affected by the temperature of the coatings [61]. Therefore, the resistance and linearity of the V versus I curve were verified at different temperatures.

The relationship between the voltage across and current through the NiCr and NiCrAlY coatings were found to be linear for all the temperatures, ranging from -25°C to 80°C, that were studied and is as shown in Fig. 15. Therefore, the coatings may be considered to be Ohmic at

any temperature between -25°C and 80°C. The curves of electrical resistance versus temperature are shown in Fig. 16. It was found that the electrical resistance and temperature have a linear relationship within the temperature range that was explored in this study. The coefficient of determination (r^2) for the regression lines of the experimental data points was at least 0.85 or greater for both coatings. Within the temperature range, the electrical resistance of the NiCrAlY coating increased by 5% from 3.52 Ω at -25°C to 3.67 Ω at 80°C. The effect of temperature on the electrical resistance of NiCr was more pronounced, with a 35% increase in the electrical resistance, from 2.69 Ω at -25°C to 3.65 Ω at 80°C. Figure 15a also shows greater variation in the slopes of the *V* versus *I* curves for NiCr, and nearly negligible variation in the slopes of the curves for NiCrAlY (see Fig. 15b). These results suggest that, for the NiCrAlY coating, the dependence of electrical resistance on temperature is weaker than in the case of NiCr. The NiCr material that is used to fabricate resistive heating wires has been shown to have resistance with a high dependence on temperature [62]. The equations of the regression lines shown in Fig. 15 were expected to present an intercept to the *V*-axis that was equal to zero, given that the values of voltage would be equal to zero when zero electrical current is applied to the samples. However, it was found that the intercept to the *V*-axis was equal to 0.3978 V for both coatings. This systematic error was due to the resolution of the measurement instruments that were used in the characterization of the electrical properties of the coating and the standard deviation of the measurements. In addition, the electrical circuit used in the measurement of the electrical resistance (see Fig. 7) comprised wires in which electrical resistance could have slightly affected the measurements of the resistance of the coatings. Regardless, due to the low electrical resistance of the wires, their effect on the experimental results is expected to be low.

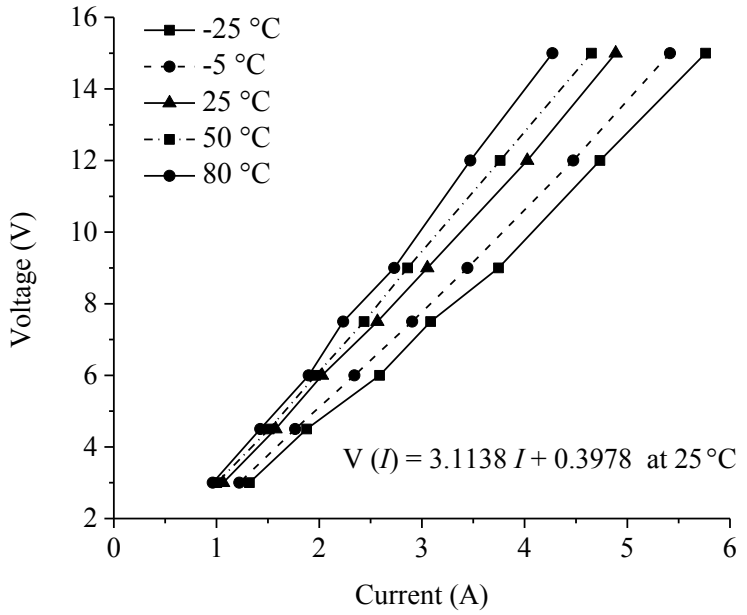

(a)

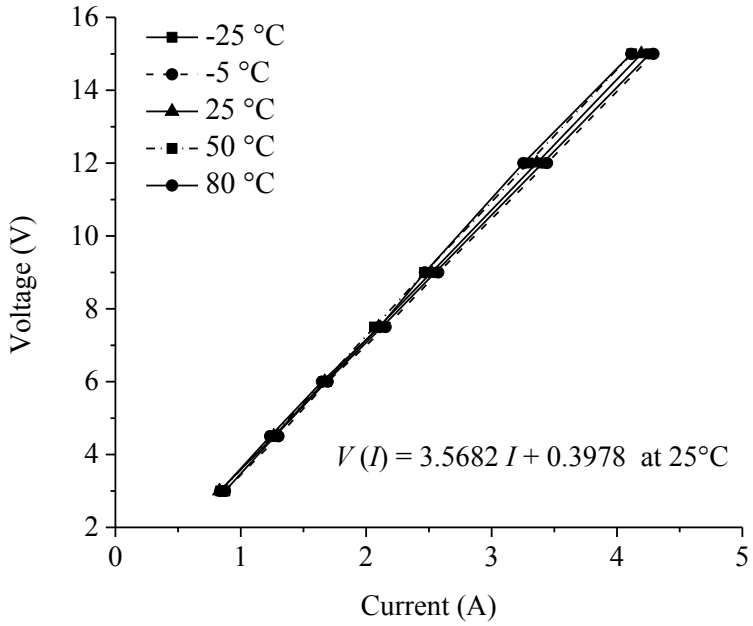

(b)

Figure 15: Voltage versus current for the **a)** NiCr and **b)** NiCrAlY coating at different temperatures

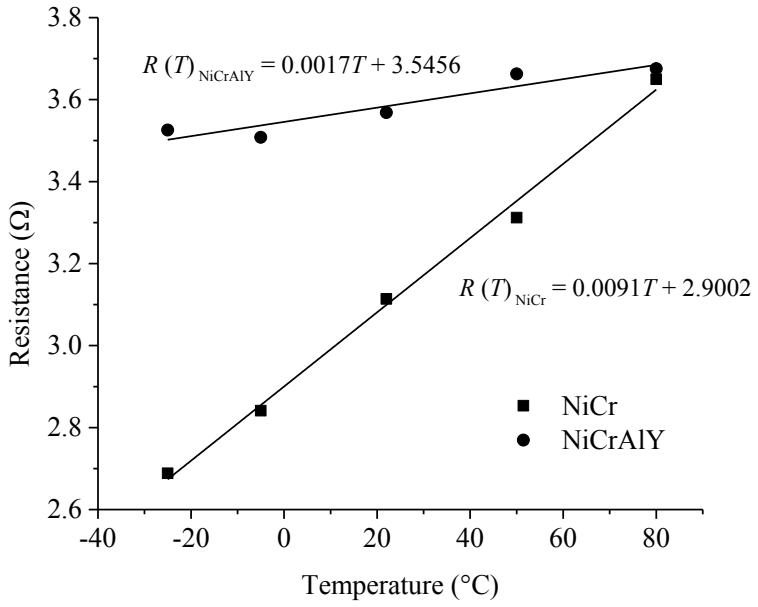

Figure 16: Resistance versus temperature for the NiCr and NiCrAlY coatings

Unlike bulk and continuous materials, flame-sprayed coatings are a porous network constituting particles, defects, and voids, and their material properties are affected by these various unique microstructural features [63, 64]. In this study, the electrical resistance, which is a property of a body that includes material properties and geometric factors, can be used to find the effective electrical resistivity of the sprayed materials. The electrical resistivity is $\varepsilon_{\text{eff}} = \frac{RA}{l}$, where R is the electrical resistance of the sample, l is the length of the sample, and A is the cross section area of the coating [44, 61]. Based on the measurements of resistance, the resistivity of the NiCr coatings at 25°C, with 6.8 vol.% porosity and thickness of 100 μm, was 5.18 x 10^{-5} Ω-m. On the other hand, the electrical resistivity of the NiCrAlY coatings at 25°C, with 1.7 vol.% porosity and thickness of 80 μm, was 4.18 x 10^{-5} Ω-m. These values for resistivity are more than one order of magnitude higher than the bulk electrical resistivity of NiCr, equal to 0.11 x 10^{-5} Ω-m

[44]. The significant increase in the electrical resistivity of the coatings compared to that of the bulk material is mainly due to the voids in the volume of the coating given that they decrease the available path in which electrons travel through the coating when electric current is applied. In addition, the high temperature in the flame during the deposition process might promote the formation of oxides that increase the effective resistivity of the coating given that oxides are ceramic materials with high electric resistivity.

4.4. JOULE HEATING TEST UNDER FREE CONVECTION CONDITIONS

Joule heating, also known as Ohmic or resistive heating, is the generation of heat in a metal as a result of the passing of electrical current through the metal. Electrical current was supplied to the coatings over 3 V, 6 V, and 12 V at ambient temperatures of -25°C, -5°C and 23°C under free convective conditions. Under free convection heat transfer, heat was lost from the coating and the uncoated FRPC surface as fluid movement due to density gradients in the air promoted the energy transfer [51, 52]. The absence of a fluid machine in free convection heat transfer produces low air velocities close to the coating and FRPC surfaces, with the majority of the air remaining stagnant. The temperatures on the coating and FRPC surfaces of the substrate samples were measured. The temperature of the surfaces increased, and was higher than that of the ambient environment due to the generation of heat by Joule heating. Figure 17 shows the temperature profiles along the NiCrAlY coating surface and along the uncoated FRPC surface of the substrates in ambient environments at 23°C, -5°C and -25°C for the various electrical powers that were applied. The distance on the horizontal axis represents the distance relative to the negative electrical terminal (at 0 mm).

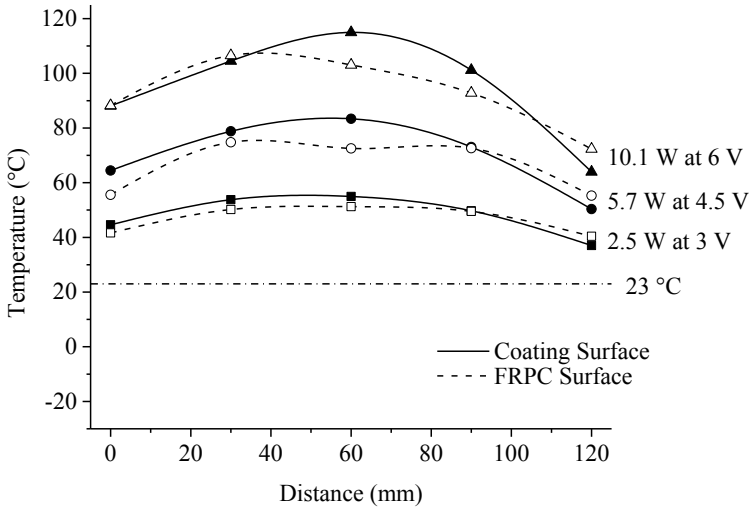
Temperature (°C)
Distance (mm)
10.1 W at 6 V
5.7 W at 4.5 V
2.5 W at 3 V
23 °C
Coating Surface
FRPC Surface

(a)

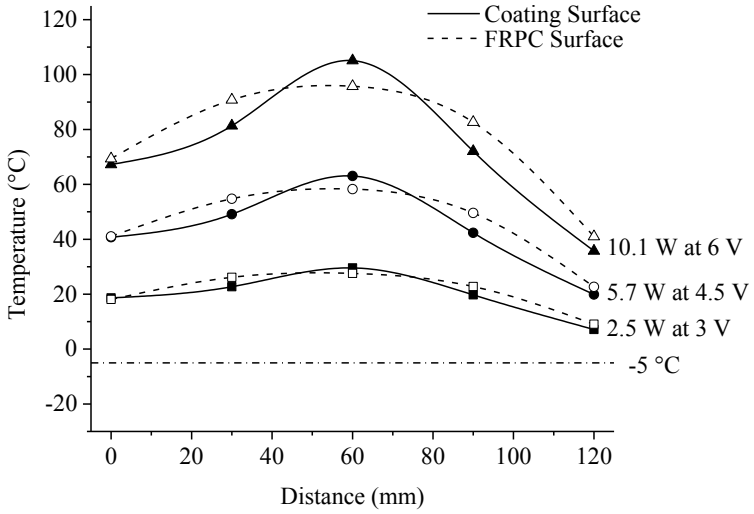
Temperature (°C)
Distance (mm)
Coating Surface
FRPC Surface
10.1 W at 6 V
5.7 W at 4.5 V
2.5 W at 3 V
-5 °C

(b)

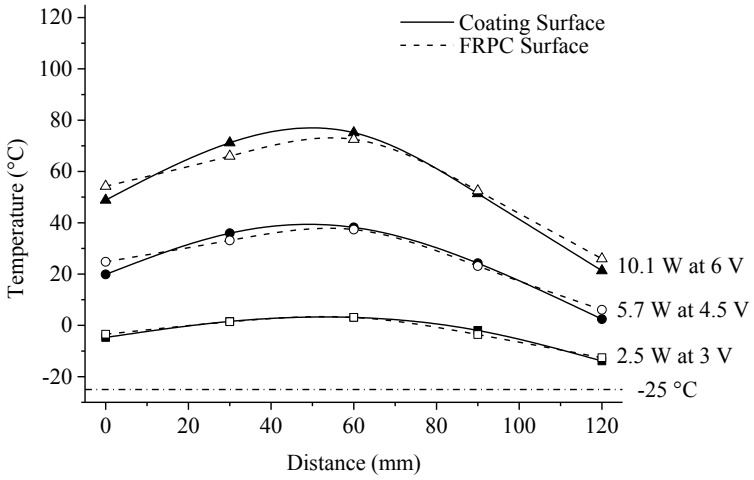

(c)

Figure 17: Temperature profiles along NiCrAlY-coated FRPC exposed to air at **a)** 23°C, **b)** -5°C, and **c)** -25°C under free convective conditions

The temperature distributions were quasi-parabolic, with the lowest temperatures at the locations at which the copper terminals were attached to the coated sample. The temperatures increased on approach to the center of the substrate sample. As shown in Fig. 17a, the minimum temperatures in the NiCrAlY coating that was held in nearly stagnant air at 23°C with an applied electrical power of 5.7 W over 4.5 V was 64°C at 0 mm and 50°C at 120 mm. The maximum temperature was 83°C at 60 mm. This represents an increase in the surface temperature of the coating of between 27°C and 60°C above the ambient temperature (23°C). In addition, Fig. 17b shows that the minimum temperatures in the NiCrAlY sample at -5°C with an applied electrical power of 5.7 W over 4.5 V were 40°C at 0 mm and 20°C at 120 mm. The maximum temperature was 63°C at 60 mm. The temperature of the coating was 24°C to 66°C greater than the ambient temperature of -5°C. Under the same applied electrical power of 5.7 W

over 4.5 V and for an ambient air temperature of -25°C, the temperature of the coating surface at the copper terminal located at 0 mm was 19°C and at the terminal located at 120 mm from the leading edge, it was 2.5°C. The maximum temperature was 38°C at 60 mm (see Fig. 17c). Over the surface, the temperature was between 27°C and 53°C greater than the ambient temperature. For all the electrical power inputs that were studied, the measured temperatures of the coatings and the uncoated, bare FRPC surfaces deviated by approximately 10% or less (see Fig. 17). As a consequence of the low local heat transfer coefficient (h), which is typical in cases of free convection, and the low thickness (ζ) of the sample, the Biot number, $\mathrm{Bi} = \frac{h\zeta}{k_c}$, of the sample in this study was small compared to unity. It has been shown that where the Biot number is less than unity, the temperature across the cross section of a structure will be uniform [51, 52]. This near uniformity of the temperature across the cross section of the coating-substrate ensemble was observed in Fig. 17.

The increase in the applied voltage generated an increase in the electrical power through the coating, resulting in increased surface temperatures of the coating and the uncoated bare FRPC. The energy generated by Joule heating depends on the resistance of the material and the electrical load that is applied. Thus, the input power increased as the voltage increased, resulting in an increase in the temperature in the sample. The maximum temperature when 2.5 W at 3 V was applied was 55°C, 83°C when 5.7 W at 4.5 V was applied, and 115°C when 10.1 W at 6 V was applied, all in an ambient environment at 23°C. A similar trend was observed in the coatings that were exposed to the lower ambient air conditions that were studied.

Absent from either the coating or uncoated, bare FRPC surfaces were evidence of hot spots. Hot spots are characterized by regions on the surface with concentrated heat flux and localized high temperatures. In anti- or de-icing applications, the occurrence of hot spots could result in areas of the surface devoid of ice accumulation, and other areas with ice accumulation as observed by Mohseni, *et al*. [25]. In addition, intense localized heat loads could potentially induce structural damage of the FRPC substrate and possible metallurgical transformations in the coating. As Fig. 17 shows for the NiCrAlY coating and FRPC surfaces, the variation in temperatures across the surfaces was gradual (smooth), without evidence of hot spots. The possible occurrence of any hot sports within the coatings on the samples would be attributed to changes of in the microstructure of the coatings due to the presence of pores or variation in coating thickness. These would produce local variations of the electrical resistance of the coating, and therefore, produce variations in the heat generated by the coating. This could be confirmed by using infrared or two-color pyrometer imaging techniques that would provide a complete temperature profile of the surface of the samples.

It was found that the difference between the temperature at any point across either the surface of the coating or the uncoated, bare FRPC and the ambient temperature, be it 23°C, -5°C or -25°C, was nearly constant. Figure 18 shows the average temperature difference between the temperature across the NiCrAlY- and NiCr-coated FRPC samples and the ambient temperature. On the NiCrAlY-coated sample, there was an increase of at least 13°C above the ambient temperature for the power condition of 2.5 W at 3 V, with a maximum increase in temperature of 95°C for the 10.1 W at 6 V condition. On the NiCr-coated sample, a minimum increase of 15°C above the ambient temperature was observed for a power of 2.9 W at 3 V. A maximum

increase in temperature of 96°C for the power condition of 11.5 W at 6 V was also observed. Given that the temperature difference between the surfaces and the ambient temperature at a given point is nearly independent of the ambient temperature, and the surface areas of the samples (A) were approximately constant, any changes in heat loss was due to variations in the local heat transfer coefficient, h that is found in Newton's Law of Cooling, $\dot{q} = hA(T_F - T_\infty)$, where $\dot{q}$ is the heat transfer rate from the surface and T_F and T_∞ are the surface and ambient temperatures, respectively. In free convection, the heat transfer coefficient is a function of surface temperature, ambient temperature, and the thermal and fluid properties of the air. The variation of temperature and temperature difference over the entire surfaces (see Figs. 17 and 18) would affect the average heat transfer coefficient, $\overline{h}$ and the total heat transfer rate from the surfaces.

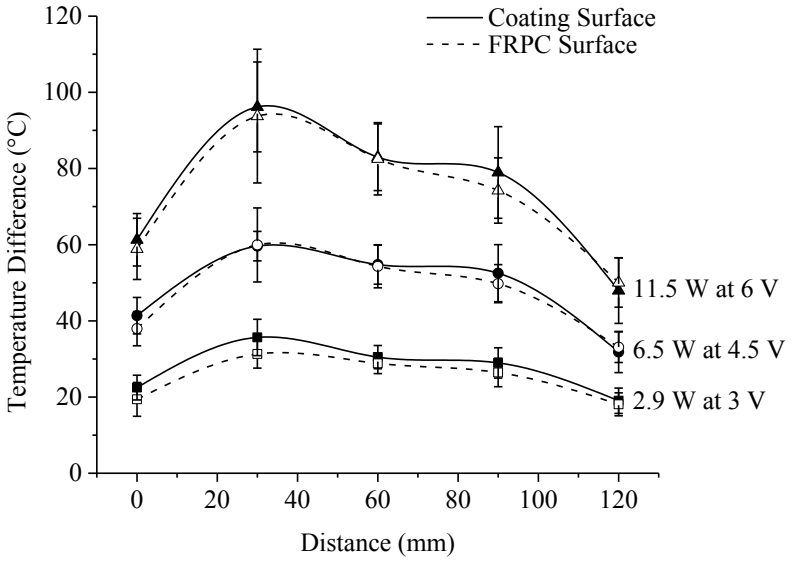

(a)

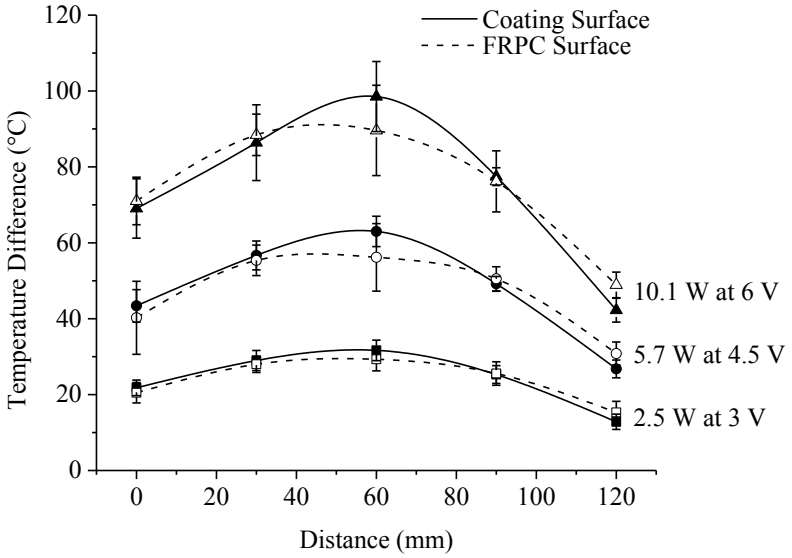

(b)

Figure 18: Average temperature differences across the **a)** NiCrAlY-coated and **b)** NiCr-coated FRPC samples under free convective conditions

A *t*-test statistic (STATISTICA for Academia, StatSoft Inc., Tulsa, OK, USA) was performed to evaluate the statistical difference between the temperature on the coating and the uncoated, bare FRPC surfaces. Unequal variances and a significance level of $\alpha = 0.05$ were used in the evaluation. A value of 0.05 was chosen because it provides a 95% confidence interval, which means that it can be reliably concluded that there is no significant difference between the temperature distribution of the coating surface and that of the FRPC surface. A significance level of 0.27 was found. This suggests that in all the experiments under the free convection condition, the temperature difference between the coating and the uncoated, bare FRPC surfaces was statistically negligible. Given that temperature variation across the coating-substrate ensemble sample was negligible, the heat conduction through the material may be assumed to be one dimensional. This approximation is valid for cases were the Biot number is small compared to unity.

As was shown in Fig. 16, the electrical resistance in the NiCrAlY coatings is higher than that of the NiCr coatings in the temperature range of -25°C to 80°C. Thus, more electrical energy from the flow of electrons in the NiCrAlY coating was transformed into heat for a given voltage. This is evidenced in Fig. 19, where the power supplied to the coating is shown to be a linear function of the average temperature difference between the temperature of the sample and the ambient temperature. The NiCrAlY-coatings required less energy than the NiCr-coatings samples to reach a given average temperature difference between the temperature of the sample and the ambient temperature in the temperature difference range between 20°C and 75°C. Given that the NiCrAlY coating produced higher surface temperatures in Joule heating under the free convective test conditions and that less material was required during the deposition and

fabrication process to obtain continuity in the coatings (see Table 1), NiCrAlY-coated FRPC substrate samples were tested further under forced convective heat transfer conditions and under the de-icing tests.

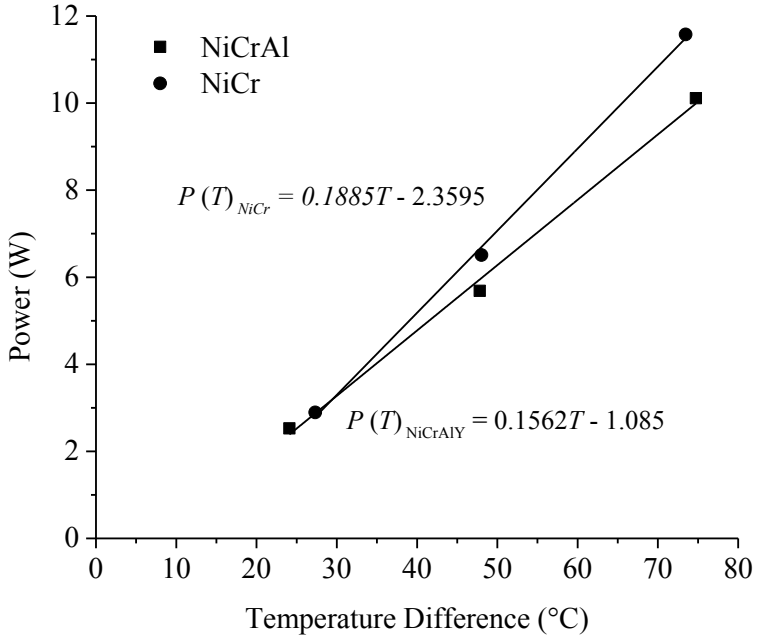

Figure 19: Power supplied versus average temperature difference for NiCr- and NiCrAlY-coated FRPC samples under free convective conditions

4.5. JOULE HEATING TEST UNDER FORCE CONVECTION CONDITIONS

Electrical current was supplied to the NiCrAlY coating over 3 V, 6 V, and 12 V at 23°C, -5°C, and -25°C ambient environment temperatures under forced convection. The fan-duct assembly shown in Fig. 9 was used. The speed of the free-stream airflow was measured to be 8.63 m/s (19.3 miles/h). This free-stream air velocity provided a conservative testing parameter value since the Canadian Wind Energy Atlas [65], and previous studies [66–68] have suggested that average wind speeds at 50 m above grade in Canada and North America are typically about

6.5 m/s (14.5 miles/h). Figure 20 shows the temperature distribution along the NiCrAlY coating and the FRPC surfaces at a room temperature of 23°C under forced convection. The temperature distribution showed a quasi-parabolic behaviour where the lowest temperatures were located at the points of the sample where the copper terminals were attached. The maximum temperature was close to the center of the sample. As described previously, no significant difference between the temperature across the cross sections of the NiCrAlY coating and the FRPC surfaces was found along the sample at different ambient temperatures under the free convective conditions. However, the temperatures in the NiCrAlY coating were significantly higher than the temperatures in the uncoated, bare FRPC surface under forced convection (see Fig. 20). The lowest temperatures in the NiCrAlY coating in an ambient at 23°C under forced convection with 5.7 W over 4.5 V of supplied power were 38°C at 0 mm and 33°C at 120 mm. The maximum temperature was 44°C at 30 mm. This represents an increase in the surface temperature of the coating of between 10°C and 21°C above the ambient temperature (23°C). On the other hand, the minimum temperatures on the FRPC surface were 29°C at 0 mm and 120 mm for the same condition of supplied power. The maximum temperature was 32°C at 30 mm. This produces a temperature difference of between 6°C and 9°C between the FRPC surface and the ambient at 23°C. There was a significant difference across the sample thickness, between the NiCrAlY coating and the FRPC surfaces. At a supplied power of 10.1 W at 6 V, the maximum temperature of the coating in an ambient at 23°C was 58°C, while that of the FRPC surface was 37°C. This represents a 21°C temperature difference across the cross section thickness of the sample. The noticeable temperature difference is due to the higher heat transfer coefficient that is typical of forced convection. The higher heat transfer coefficient produced Biot numbers that

were likely greater than unity, which would indicate the occurrence of temperature variation across the cross section of the coating-FRPC ensemble.

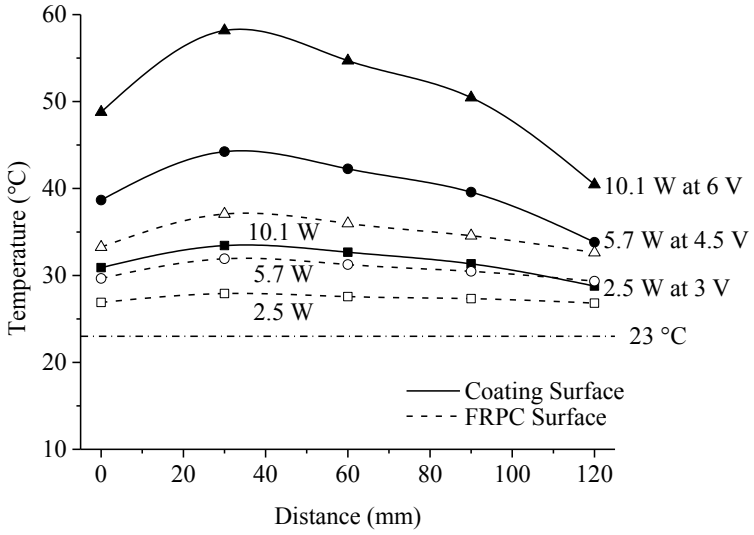

Figure 20: Temperature profiles along NiCrAlY-coated FRPC exposed to air at 23°C under forced convective conditions

It was found that the maximum temperature on either the coating or the FRPC surfaces of the samples exposed to forced convection was located at 30 mm (see Fig. 20) from the leading edge (or negative terminal). On the other hand, the maximum temperature of the surfaces of the samples exposed to free convection was located at approximately 60 mm, close to the center of the sample. This difference in the location of the maximum temperature is possibly due to the development of and transition to a turbulent boundary layer on the surface of the sample when the air was flowing over the surfaces under the forced convection condition. Within the boundary layer, the flow regime varied along the length of the sample, changing from laminar

flow to turbulent flow. For forced convective flow, the Reynolds number, $\mathrm{Re} = \frac{\rho_A u}{\mu}$, is used to characterize the flow regime. The free-stream velocity (u) will be approximately constant, but the density (ρ_A) and dynamic viscosity (μ) of the air will vary with temperature. Transition from laminar to turbulent flow over smooth flat plate surfaces occurs at approximately $\mathrm{Re}_x \approx 5 \times 10^5$ [69]. At 30 mm from the leading edge of the FRPC-coated sample plate, the Reynolds number is on the order of $\mathrm{Re} \approx 2 \times 10^4$. While the value of the Reynolds number suggests laminar flow, tripping of the flow to turbulence with a rough surface or other perturbations such as flow unsteadiness or curvature of the plate will initiate transition from laminar to turbulent flow at lower Reynolds numbers and at shorter distances from the leading edge [69]. It has been shown that due to the higher shear stresses in turbulent flow, the convective heat transfer coefficient will increase [52, 54]. This will in turn increase heat transfer losses from the surface, resulting in lower surface temperatures in the region of the sample that is exposed to turbulent boundary layer flow.

Figure 21 shows the average difference between the temperatures of the NiCrAlY coating and the uncoated, bare FRPC surfaces of the substrate and the ambient temperature under forced convective conditions at -25°C, -5°C, and 23°C. The semi-parabolic shape of the temperature profiles on the coated surface was consistent with that which was found in the tests under free convection conditions. However, the temperature increase was significantly lower. As shown in Fig. 21, for example, the minimum temperature differences on the coating surface, where 5.7 W over 4.5 V applied, was located at the edges of the samples, and were 13°C at 0 mm and 9°C at 120 mm. The maximum temperature increase was 18°C above the ambient

temperature for the same test. On the other hand, the temperature on the bare, uncoated FRPC surface increased slightly above the ambient environment temperature, achieving, at most, a 12°C temperature difference for the condition where 10.1 W over 6 V was applied to the coating. The maximum temperature on the coating surface was 32°C greater than the ambient temperature for the same condition of applied electrical power. This represented a difference of 20°C across the substrate. The large variation of temperature across the thickness of the coating-FRPC ensemble was due to the increase in the convective heat transfer coefficient, h, caused by the higher air velocity, which is typical of forced convection conditions. Unlike the free convection condition, where the heat transfer coefficient was lower, producing a more uniform temperature across the cross-section of the coating-FRPC ensemble (see Fig. 17), a lower Biot number, and a one-dimensional heat transfer problem, under the forced convection condition, the non-uniform temperature across the coating-substrate system and a higher Biot number, which may likely be greater than unity, would make for a multi-dimensional heat transfer problem.

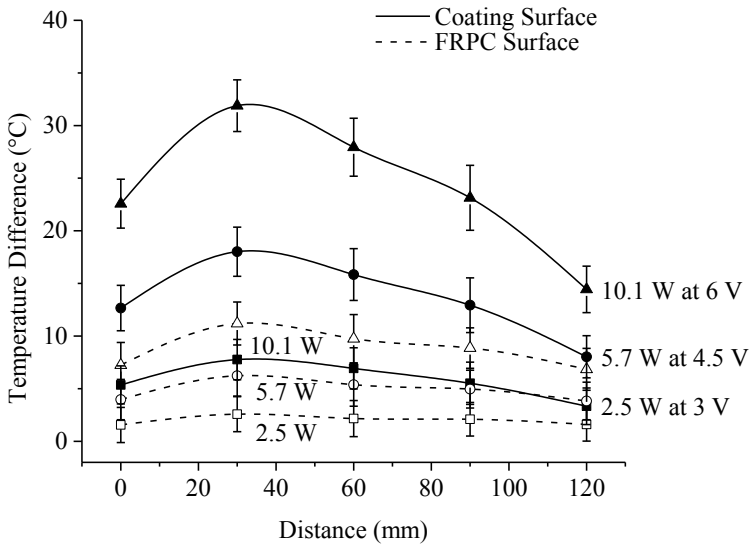

Figure 21: Average temperature difference across the NiCrAlY-coated and bare, uncoated FRPC surfaces under forced convective conditions

The power that was supplied to the coating is shown in Fig. 22 as a linear function of the average temperature differences between the temperatures of the surfaces of the NiCrAlY coating and the bare, uncoated FRPC and the ambient temperature under forced convection. It was found that an increase in the temperature of the FRPC above room temperature required a higher input power than that required for the increase in temperature of the coating. For example, an increase of 10°C in the surface temperature of the coating above the ambient temperature required approximately 4.3 W of power to be applied across the copper terminals and coating (see Fig. 22). On the other hand, 12.3W of power was required in order to have the same increase in temperature of the FRPC surface above room temperature.

It was found that the rate of change of the power supplied to the NiCrAlY coating varied between conditions of exposure to free convection and forced convection. This is evidenced in the curve fit equations of the power versus temperature difference of the NiCrAlY coatings in Figs. 19 and 22. The smaller slope of the curve (0.1562 W/^{o}C) in Fig. 19 implies that the coating required a tempered increase of the applied power in order to have an increase in the temperature under free convective conditions than under the forced convection condition where the slope shown in the equation (0.4166 W/^{o}C) is higher (see Fig. 22). The increase in the heat transfer coefficient due to the flow of air over the coating surface during forced convection generated an increase in the heat transfer from the surface to the environment, requiring more rapid increases in power to maintain the temperature differences.

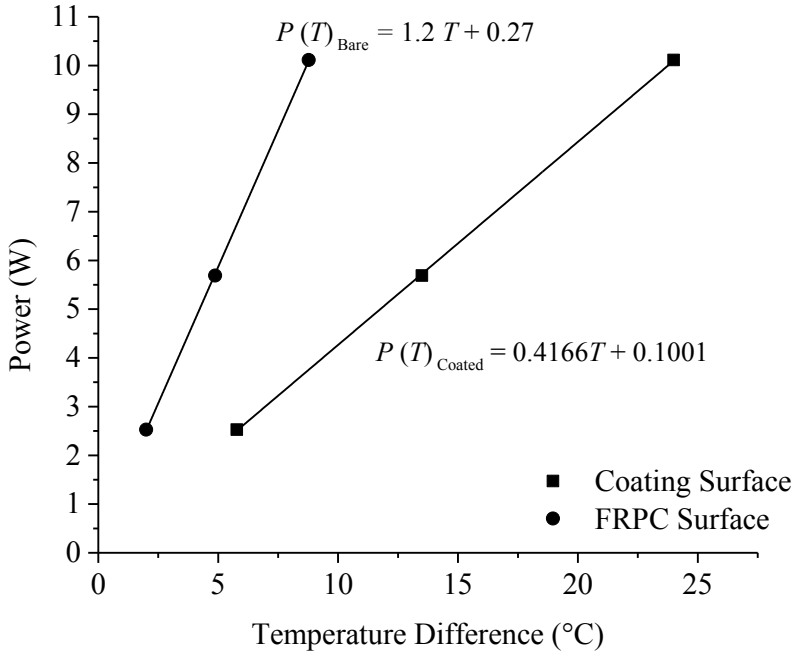

Figure 22: Power supplied versus average temperature difference for NiCrAlY-coated and bare, uncoated FRPC surfaces under forced convective conditions

4.6. DE-ICING TEST AND MODEL VALIDATION

4.6.1. Heating of the Ice and FRPC Sample

The accumulation of ice and the performance of the coatings as de-icing systems were determined and investigated, respectively, in this study. Table 3 summarizes the results for all the experiments that were performed in this work. It was found that the thickness of the ice on the surface of the FRPC sample increased as the ambient temperature decreased from -5°C to -25°C. A thickness of 2.3 mm at an ambient temperature of -5°C was observed, with the thickness of the layer of ice over the FRPC sample increasing by approximately 1 mm for every 10°C decrease in temperature over the range of temperatures that were evaluated in this study. Lower ambient room temperatures have been previously found to increase the formation of ice in experiments and field measurements [10, 18].

Table 3: Heating and melting time for ice layers at different ambient temperatures

Ambient Temperature	Ice Thickness	Applied Power	FRPC Temperature	Ice Heating Time	Ice Melting Time
°C	mm	W	°C	s	S
-5 ± 2	2.3 ± 0.06	1.64	-5 ± 2	46 ± 5	557 ± 12
-15 ± 2	3.4 ± 0.1	5.53	-13 ± 2	60 ± 11	363 ± 15
-25 ± 2	4.4 ± 0.2	9.61	-17 ± 4	77 ± 8	260 ± 12

Transient temperature traces of the bare FRPC surface, coating surface, ice surface, and the ambient room temperature were generated for various ambient temperatures. Figure 23 shows the

transient temperature trace of the FRPC, coating, and ice when the ambient temperature was set to -15°C. Ambient temperatures of -5°C and -25°C were also explored, and similar trends to those shown in Fig. 23 were observed. The ambient room temperature fluctuated around the set-point temperature (see Fig. 23) due to the on-off configuration of the control unit in the cold room. Different stages were identified in the traces shown in Fig. 23. The trace for the ice shows an initial heating stage where the layer was heated from an initial temperature of -15°C to its melting temperature of 0°C. The time that was necessary for the ice to change from the initial temperature to the melting temperature, hereafter referred to as heating time, was 60 seconds. Within the heating process, the temperature of the coating, at the base of the ice layer, and the temperature of the outer surface of the ice were approximately the same, with a maximum difference of 2°C.

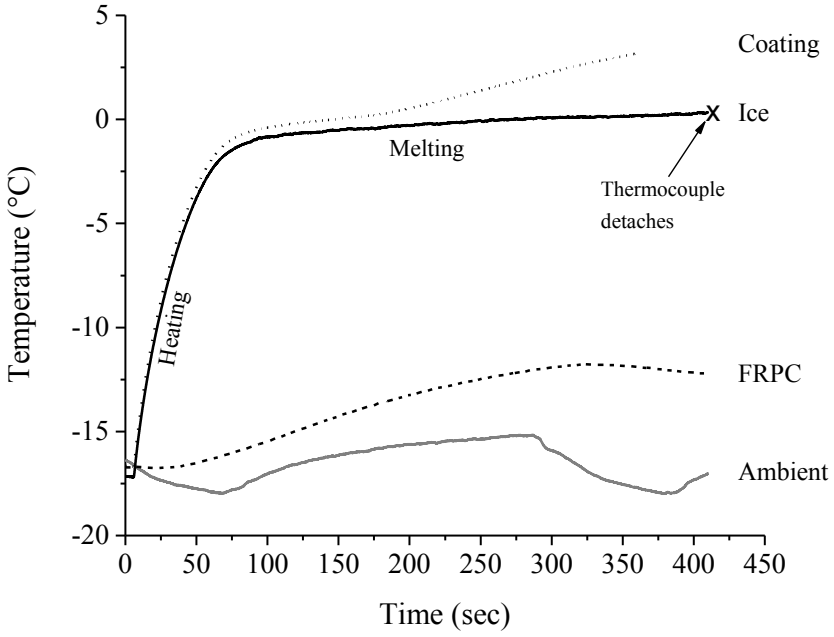

Figure 23: Transient temperature traces from the de-icing test at -15°C ambient room temperature

The absence of spatial variation in the temperature in the ice may be explained by considering typical values of the Biot number. In this study, a fan in the air duct (see Fig. 9) was used to move cold air over the free surface of the ice to produce forced convective heat transfer. The average convective heat transfer coefficient, h, is determined analytically from Pohlhausen's solution for flow over flat plates [52], and is given as

$$h = \frac{k_A}{l}\left(0.664\,\mathrm{Re}^{\frac{1}{2}}\,\mathrm{Pr}^{\frac{1}{3}}\right), \qquad 0.6 < \mathrm{Pr} < 10. \tag{36}$$

Equation 36 is valid for Reynolds numbers that are lower than 5 x 10^5, where the flow is laminar over the flat plate [52]. In this study, with a mean free-stream air velocity of 8.63 m/s, a substrate length of 0.12 m, and air properties at -15°C, the Reynolds number was approximately 8.5 x 10^4. Hence, from Eq. 36, the average convective heat transfer coefficient over the ice free surface at -15°C was approximately 34 W/m^2-K. Changes in air properties at -5°C and -25°C would produce marginal changes in the average heat transfer coefficient. The Biot number, $\mathrm{Bi} = \frac{h\delta}{k_s}$, with an ice thickness of approximately 5 mm and thermal conductivity of 2.2 W/m-K [53] , was approximately 0.08. Since the Biot number was less than 0.1, the assumption of lumped-capacity with respect to the ice is valid. The small value of the Biot number also supports the assumption that the temperature of the layer of ice does not vary spatially and only depends on time. This was equally observed in the experiments in this study. The convective heat transfer coefficient, h, can be used to find the heat loss by means of heat convection through the layer of ice and compared to

that lost by radiation. For instance, the convective energy loss of a layer of ice at melting point of 0°C inside a cold room at temperature of -10°C was 0.81 W/m^2. This is significantly higher than what was estimated for heat loss by means of radiation (0.1 W/m^2). Given that the radiative loss was approximately 12% that of the convective loss, it was ignored in the model since inclusion of radiation into the model would have resulted in a non-linear problem.

As a consequence of decreasing the ambient temperature, it was observed that increased power across the NiCrAlY coating was required in order to heat and, eventually, melt the ice on the FRPC sample surface. As observed from the results shown in Table 3, lower ambient temperatures increased the heating time of the ice given that longer times were required to increase the initial temperature to the melting temperature over a larger temperature difference. In addition, according to Newton's Law of Cooling, the larger difference between the ambient temperature and the temperature of the ice during the heating process produced greater convective heat loss from the layer of ice to the environment. This eventually increased the heating time since a portion of the total heat from the coating was transferred to the environment and was unavailable for heating the ice. Fundamentally, the process of heating to change the temperature of the ice is coupled to the ability of the ice to store the energy originating from the coating. In the heating process of this study, the ability of the ice to store energy was stultified by the lower ambient temperature and the forced convection heat transfer at the free surface of the ice.

The variation in power in the NiCrAlY coating also affected the energy transfer through the FRPC substrates. At -5°C, with 1.64 W of applied power at the coating, the FRPC did not present

any variation in temperature from that of the ambient air. This was due to the low thermal conductivity of the FRPC substrate of 0.3 W/m-K and the low power that was generated by the coating. These effects, combined, produced a situation in which the energy from the coating was not effectively conducted through the thickness of the FRPC sample. However, as the ambient temperature decreased and the power applied to the coating was increased, the temperature of the composite surface increased (see Table 3). The difference between the temperature of the FRPC surface and the ambient temperature produced heat loss that was directly proportional to the temperature difference in accordance with Newton's Law of Cooling. The thermal properties of the substrate on which the coatings are deposited are important for the performance of the coatings as de-icing elements. Substrates with high thermal conductivity would rapidly conduct the energy generated in the coating, decreasing the amount of energy transferred to the ice. Therefore, low thermal conductivity materials such as polymers and polymer-based composites would be better suited as substrates for coatings that are used as anti- and de-icing elements.

The prediction of the heating time of the ice on the FRPC sample surface was dependent on the transient temperature distribution in the solids. The heating time was estimated by using Eq. 8 for different ambient temperatures. The heating time was measured as the time that was required for the temperature of the free surface of the ice to increase from the initial temperature, T_i, to the melting point, T_f. Figure 24 shows that the heating time that was predicted by the lumped-capacity model of Eq. 8 increased as the ambient room temperature decreased. The model predictions of heating time were within 20% of those that were measured experimentally. This difference is mainly due to the assumptions that were made in the formulation of the heat transfer model that lead to Eq. 8. Equation 4 shows that the heat that is transferred from the coating to the ice was the

difference between the power generated by the coating, $P = \frac{V^2}{R}$, and the heat transferred through the FRPC bare surface to the ambient, $hA(T_F - T_\infty)$. The heat transferred by convection through the FRPC, was assumed to be steady during all the experiments, however, as is shown in Fig. 23, the temperature of the FRPC surface was transient. Given that the difference between the surface temperature of the FRPC and the ambient air increased with time, the heat lost by convection from the surface was not steady, and likely increased with time. Therefore, by using an average FRPC surface temperature in Eq. 8 that was lower than the actual surface temperature of the FRPC at various instances during the heating process, the model implicitly assumed lower heat loss from the FRPC surface in Eq. 4, resulting in higher energy input into the ice from the coating, thus predicting heating times that were lower than those obtained from experiment (see Fig. 24). In addition, Eq. 36 that was used in estimating the convective heat transfer coefficient is a correlation equation in which the constants have been previously obtained experimentally [54]. While Eq. 36 is applicable to the experiments performed in this work, the experimental conditions that were used in estimating the constants in Eq. 36 could be different to the ones in the experiments of this work, which could contribute to increasing the deviation between the experimental results and those predicted by the heating model.

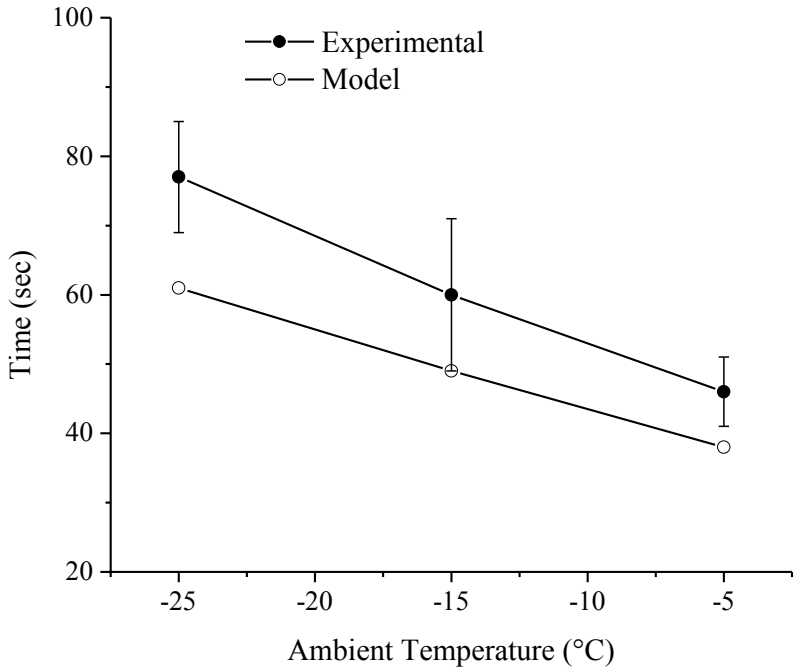

Figure 24: Experimental and predicted heating times of the ice at different ambient temperatures

4.6.2. Melting of the Ice

The uniform heating of the ice to the melting point was followed by melting, forming a system with an independent liquid and solid phase. The liquid-solid interface moved from the ice-coating interface towards the free surface of the ice. Figure 23 shows that during melting and movement of the liquid-solid interface from the coating to the ice free surface, there was a solidification plateau at the melting point of approximately 0^{o}C in the temperature trace of the surface of the ice. Once the liquid-solid interface arrived at the free surface, the thermocouple that was attached to the free surface detached since the material was no longer solid. This indicated completion of the melting process of the ice.

Figure 25 shows the melting time, which is the time required for the liquid-solid interface to reach the free surface of the ice, as a function of the ambient temperature. The figure shows the results in terms of dimensional and non-dimensional parameters. The Fourier number, $\mathrm{Fo} = \frac{\alpha_{\mathrm{L}} t}{\delta^2}$, was used to represent the non-dimensional melting time, and a non-dimensional temperature, $\theta = \frac{T_{\mathrm{f}} - T_{\infty}}{T_{\mathrm{f}}}$, where T_{f} and T_{∞} are given in Kelvin, was used to represent the non-dimensional ambient temperature. Table 3 and Fig. 25a show that the melting time decreased as the ambient temperature decreased. Due to lower ambient temperatures, an increase in the applied power was required to melt the layer of ice on the coated FRPC sample, which resulted in lower melting times. Given that the melting process is isothermal, the energy that is produced in the coating does not change the temperature of the ice on the samples and is used to change the phase of the material. As can be intimated from Eqs. 33 and 35, an increase in the applied power would produce an increase in the velocity of the liquid-solid interface, producing a reduction in the melting time. The Fourier number, Fo, is the ratio of the conductive heat transfer and the heat stored in a body [70]. Figure 25b shows that the Fourier number, Fo, decreased as the ambient temperature decreased, as indicated by an increase in the non-dimensional temperature. All the experiments in this study produced Fourier numbers that were greater than 1. This indicates that the heat that is generated by the coatings was mainly conducted through the liquid-solid layers to the environment, and proportionally less heat was stored in the water and ice. The difference between the heat that was conducted through the liquid and solid phases of the water and the heat that was stored in the water is more pronounced when the initial ice thickness is small such as under an ambient temperature of -5°C (see Table 3), which is equivalent to a non-dimensional temperature of 0.018 in Fig. 25b. Due

to its low thickness, the ice on the FRPC sample provided reduced thermal resistance to heat conduction, hence facilitating energy transfer through the layer and increasing the Fourier number. As the thickness of the ice on the FRPC samples increased and the melting time decreased due to the larger applied powers, the Fourier number in the experiments with higher non-dimensional temperatures (that is, lower dimensional temperatures) decreased.

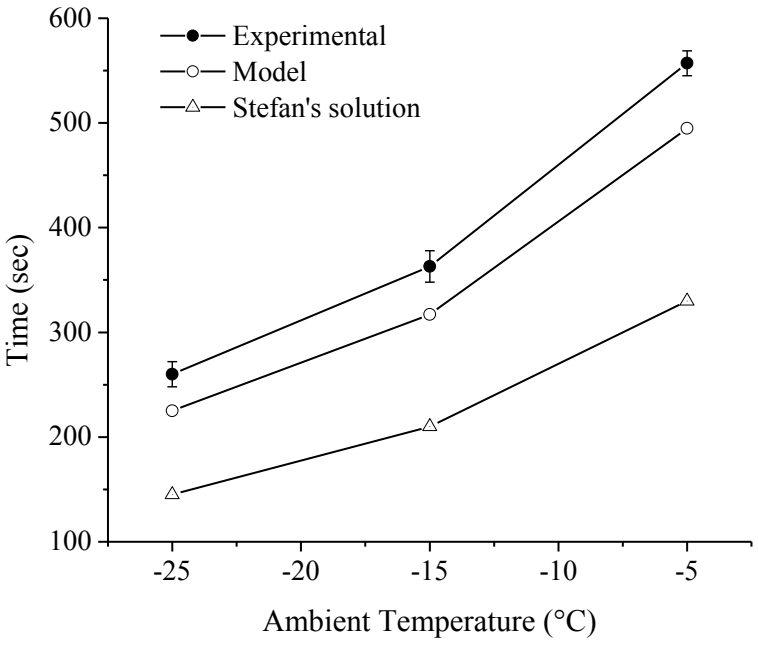

(a)

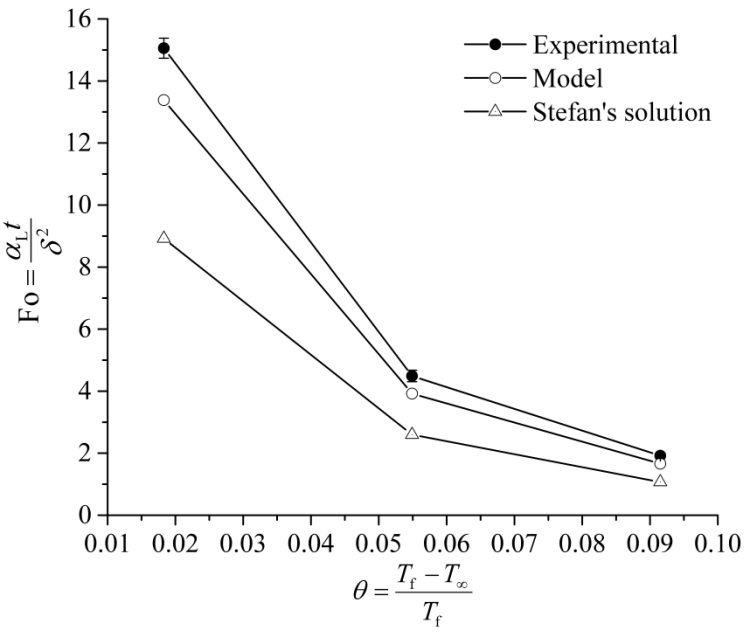

(b)

Figure 25: Experimental and predicted **a)** dimensional and **b)** non-dimensional melting time of the ice at different ambient temperatures

The melting times, as estimated by Eq. 33 for the finite length-scale model and Eq. 35 from Stefan's solution, is shown in Fig. 25, with both models predicting the same trend in melting times as a function of ambient temperature. Table 4 presents the values of the properties of liquid water that were included in Eqs. 33 and 35. The melting times that were predicted by the finite length-scale model of Eq. 33 were in closer agreement with the experimentally measured melting times to within 15%. The predictions of Stefan's solution of Eq. 35 deviated by as much as 45%. The large deviation between the predictions of the model upon which Stefan's solution is based and the experimental results is due to the assumption in the model that the solid ice layer is semi-infinite compared to the liquid phase during the melting process. This assumption becomes invalid as the thickness of the liquid layer increases as the melting process proceeds. The finite length-scale model of Eq. 33 avoids this assumption and utilizes the finite thickness of the ice to establish the time when the interface location, $x_i(t)$, traverses the finite thickness of the ice.

Table 4: Properties for liquid water [54, 71]

Property	**Value**
Melting point, T_f	0°C
Thermal diffusivity, α_L	0.143×10^{-6} m^2/s
Specific heat capacity, $c_{p,L}$	4200 J/kg-K
Density, ρ_L	1000 kg/m^3
Thermal conductivity, k_L	0.56 W/m-K
Latent heat of fusion, $\hbar$	334,000 J/kg

The effect of the lower ambient temperatures and higher power input from the coating into the ice was to induce an increase in the speed of the liquid-solid interface, $\frac{dx_i}{dt}$, during the melting process. In this case, the increase in energy from the coating to the melting ice accelerated the melting process. The increase in the speed of the liquid-solid interface resulted in a decrease in the melting time of the ice. Figure 26 shows a curve of the speed of the liquid-solid interface, as determined from the predictions of Eq. 33 for $x_i(t)$, as a function of the applied power across the coatings. The slope of the curve of the liquid-solid interface location, $x_i(t)$ as a function of time was fitted to a line by using a simple linear regression in which the constant of proportionality was the speed of the liquid-solid interface and the coefficient of determination (r^2) for the regressions was at least 0.97 or greater. As shown in Fig. 26, the speed of the liquid-solid interface increases as the applied power is increased. The speed of the liquid-solid interface increased by nearly an order of magnitude from 0.004 mm/s when the applied power across the coating was 1.64 W to 0.01 mm/s when 9.61 W of power was applied. The model predicted the trend and values of the experimental results to within 15%. Figure 26b shows that as the ambient room temperature decreased, the deviation between the model prediction of the speeds of the liquid-solid interface and those of the experiments increased. While the model of Eq. 33 factors in the heat loss from the FRPC sample due to convection, it does not include heat loss from the exposed free surface of the ice. In the experiments, the heat loss from the ice surface will increase as the ambient temperature decreases and the temperature difference between the ambient air and the ice surface increases. This will cause the observed deviation between the model and experimental results.

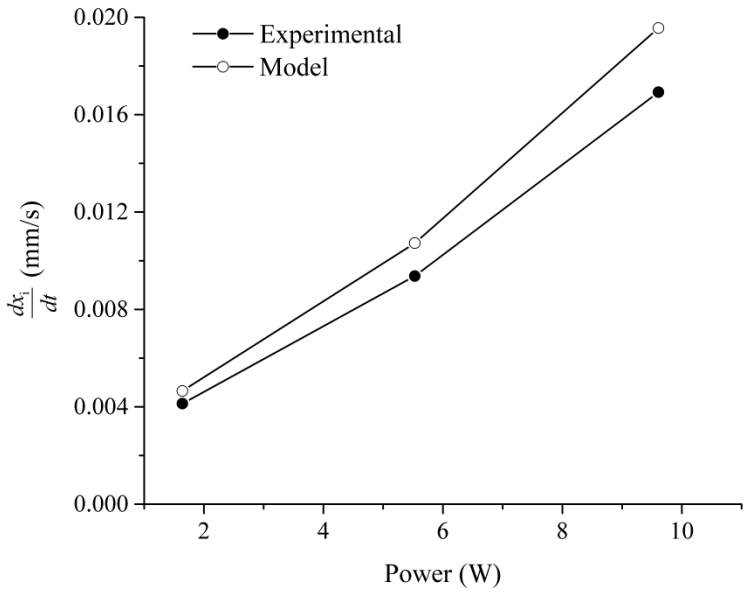

(a)

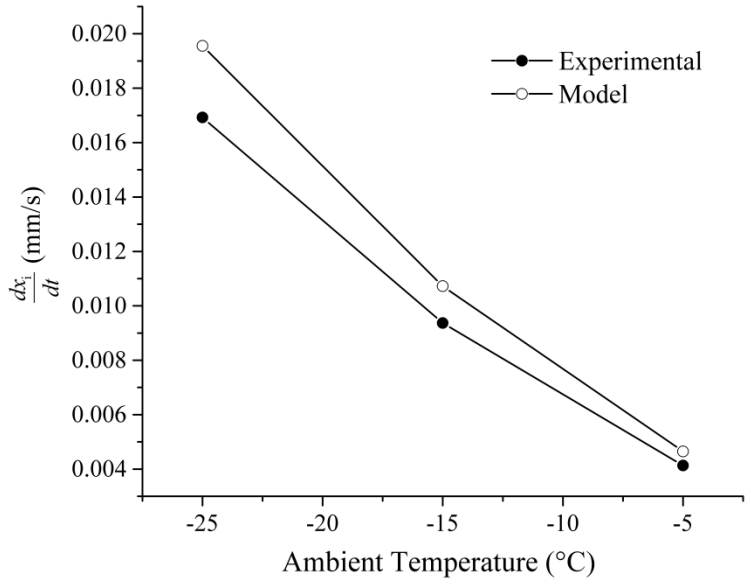

(b)

Figure 26: Velocity of the liquid-solid interface at different a) applied powers and b) ambient temperatures

5. CONCLUSIONS

In this study, the feasibility of using metallic flamed-sprayed coatings as heating elements in FRPC structures was investigated. A method to fabricate the flame-sprayed heating elements was presented. Given that the flame spray process uses a high-temperature heat source to deposit the material powder, degradation in the FRPC could possibly occur. This study presented substrate preparation and spray parameters for the deposition of NiCr and NICrAlY powders, where no degradation of the polymer-based substrate due to the high temperature exposure was found.

The performance of the coating as heating elements was verified at different temperatures under free and forced convection conditions. By applying electrical current to the coatings, the temperature in the samples was at least 15°C above the ambient temperature when no air was flowing over the sample. Under this condition, the temperature in the coating and substrate were found to be approximately equal. Under the forced convection condition, the coating temperature was at least 5°C above the ambient temperature. However, the temperature on the uncoated, bare FRPC surface was approximately the same as the ambient temperature, presenting a maximum difference of 10°C when 10.1 W of power at 6 V was applied. Under the same conditions of power, a maximum increase of the temperature of the coating of 30°C was observed.

It was found that the temperature across the cross section of the coating and the FRPC substrate was dependent on the mode of heat transfer and the flow regime of the fluid to which the surfaces were exposed. In addition, the Biot number was used to qualify the temperature variation and characterize the dimensionality of the temperature distribution in the ensemble. The results of the study suggest that, when exposed to free convective heat transfer conditions, the temperature distribution in the heated coating and FRPC layer may be treated as one dimensional. When the ensemble is exposed to forced convection heat transfer conditions, the temperature distribution is multi-dimensional.

The models that predicted the heating and melting behavior of the ice predicted values of heating and melting time with close agreement with the experimental results. In the case of melting of the ice, the well-established Stefan solution for a semi-infinite medium was applied to estimate the melting time of the ice, and significant deviations between the predictions of the model based on Stefan's solution and the experimental results were observed. These results confirmed that the assumption of a semi-infinite extent for a finite length-scale melting problem was not valid and required a solution that was based on a finite length-scale.

The speed of the liquid-solid interface was determined and used to explicate the impact of ambient temperature and heat generated from the coating on melting of the ice in the de-icing process. The loss of energy from the free surface of the ice and the transient variation of energy loss from the FRPC substrate surface were proposed as explanations for variations in the melting times that were obtained from the finite length-scale model and the experiments. The

finite length-scale model could be refined by considering the ice and FRPC substrate as a bi-layered composite medium with the coating as an interface heat source and applying the orthogonal expansion technique and the separation of variables method to determine the temperature distribution in the solids and the melting time in the ice.

6. FUTURE WORK AND RECOMMENDATIONS

Further work in developing a transient heat conduction model with phase change that includes the heat transferred from the coating to the FRPC is required. The formulation of a one-dimensional composite medium model can lead into the prediction of the transient temperature of the FRPC plate and the ice during the deicing process. One-dimensional composite medium models can be solved using the orthogonal expansion technique as described by Özişik [72].

The plate-shaped samples that were used in this study provided an initial approach to the study of flame-sprayed metallic coatings as heating elements for FRPC structures. Moreover, the exploration of different shaped samples, e.g. airfoil-shaped samples, could provide a better understanding of the performance of the coatings as anti- and de-icing systems for that application.

In addition, the coating deposition was done over a rectangular-shaped sample, covering the entire sample surface. However, the deposition of patterns that do not completely cover the sample surface could be used in exploring the heating of structures with larger area. Patterns of coatings with smaller cross-sectional areas that are used to metallize the structures could produce more heat during Joule heating.

The exploration of new shapes could result into more potential applications of the flame-sprayed heating elements. For instance, flame-sprayed coatings could be used as heat tracers and de-icing elements in FRPC pipes that may be considered as alternatives to steel pipes in applications where corrosion and wear are particularly problematic.

7. REFERENCES

[1] N. Dalili, A. Edrisy, and R. Carriveau, A Review of Surface Engineering Issues Critical to Wind Turbine Performance, Renew. Sustain. Energy Rev., 2009, 13(2), p 428-438.

[2] S.A. Kalogirou, Wind Energy Systems, *Solar Energy Engineering*, 2nd ed., Elsevier Inc., 2014 (Oxford), p 735-750.

[3] P.J. Schubel, and R.J. Crossley, Wind Turbine Blade Design, Energies, 2012, 5(12), p 3425–3449.

[4] M. Ritter, Z. Shen, B. López, M. Odening, and L. Deckert, Designing an Index for Assessing Wind Energy Potential, Renew. Energy, 2015, 83(11), p 416–424.

[5] Global Wind Eenergy Council, "Global Wind Report 2014", Global Wind Energy Council, Brussels, Belgium, 2014.

[6] Global Wind Eenergy Council, "Global Wind Report 2013", Global Wind Energy Council, Brussels, Belgium, 2013.

[7] B. Tammelin, M. Cavaliere, H. Holttinen, C. Morgan, and H. Seifert, "Wind Energy Production in Cold Climate (WECO)", Finnish Meteorological Institute, Helsinki, Finland, 2000.

[8] T. Laakso and E. Peltola, "Wind Energy in Cold Climates-IEA Wind Energy Annual Report", International Energy Agency-Wind Energy, Helsinki, Finland, 2005.

[9] S. Barber, Y. Wang, S. Jafari, N. Chokani, and R.S. Abhari, The Impact of Ice Formation on Wind Turbine Performance and Aerodynamics, J. Sol. Energy Eng., 2011, 133(1), p 1–9.

[10] A.G. Kraj, and E.L. Bibeau, Phases of Icing on Wind Turbine Blades Characterized by Ice Accumulation, Renew. Energy, 2010, 35(5), p 966–972.

[11] Y. Li, F. Feng, S.M. Li, W.Q. Tian, and K. Tagawa, Wind Tunnel Test on Icing on a Straight Blade for Vertical Axis Wind Turbine, Adv. Mater. Res., 2011, 301(1), p 1735–1739.

[12] T. Hu, H. Lv, B. Tian, and D. Su, Choosing Critical Ice Shapes on Airfoil Surface for the Icing Certification of Aircraft, International Symposium on Aircraft Airworthiness, 3rd ed., Nov 19-21, 2013 (Toulouse, France), Elsevier B.V., Procedia Eng., 2014, p 456–466.

[13] B. Rooks, Robot Spraying of Helicopter Rotor -Blade Ice Protection System, Ind. Robot An Int. J., 2001, 28(4), p 313–317.

[14] O. Parent, and A. Ilinca, Anti-Icing and De-Icing Techniques for Wind Turbines: Critical Review, Cold Reg. Sci. Technol., 2011, 65(1), p 88–96.

[15] W.J. Jasinski, M.S. Selig, M.B. Bragg, and N. Shawn C, Wind Turbine Performance Under Icing Conditions, J. Sol. Energy Eng., 1998, 120(2), p 60–65.

[16] F. Lamraoui, G. Fortin, R. Benoit, J. Perron, and C. Masson, Atmospheric Icing Impact on Wind Turbine Production, Cold Reg. Sci. Technol., 2014, 100(1), p 36–49.

[17] L. Talhaug, G. Ronsten, R. Horbaty, I. Baring-Gould, A. Lacroix, E. Peltola, and T. Laakso, “Study on Wind Energy Projects in Cold Climates”, International Energy Agency Programme, Helsinki, Finland, 2005.

[18] P. Antikainen, and S. Peuranen, Ice Loads-Case Study, BOREAS V Cold Climate Conference, 5th ed., Nov 29 - Dec 1, 2000 (Levi, Finland), Finnish Meteorological Institute, 2000, p 1–7.

[19] C. Antonini, M. Innocenti, T. Horn, M. Marengo, and A. Amirfazli, Understanding the Effect of Superhydrophobic Coatings on Energy Reduction in Anti-Icing Systems, Cold Reg. Sci. Technol., 2011, 67(2), p 58–67.

[20] T. Laakso, I. Baring-Gould, M. Durstewitz, R. Horbaty, A. Lacroix, E. Peltola, G. Ronsten, L. Tallhaug, and T. Wallenius, “State of the Art of Wind Energy in Cold Climates”, VTT Technical Research Centre of Finland, Espoo, Findland, 2010.

[21] C. Mayer, A. Ilinca, G. Fortin, and J. Perron, Wind Tunnel Study of Electro-Thermal Deicing of Wind Turbine Blades, Int. J. Offshore Polar Eng., 2007, 17(3), p 182–188.

[22] H. Seifert, Technical Requirements for Rotor Blades Operating in Cold Climate, BOREAS VI Wind Energy Conference, 6th ed., Apr 9-11, 2003 (Levi, Finland), Prod. Cold Clim., 2003, p 1-13.

[23] R. Horbaty, Wind Energy in Cold Climates - The Swiss Experience, BOREAS VII Cold Climate Conference, 7th ed., Mar 7-8, 2005 (Levi, Finland), Boreas Conference, 2005, p 1–10.

[24] Battisti, Baggio, and Fedrizzi, Warm-Air Intermittent De-Icing System for Wind Turbines, Wind Eng., 2006, 30(5), p 361–374.

[25] M. Mohseni, and A. Amirfazli, A Novel Electro-Thermal Anti-Icing System for Fiber-Reinforced Polymer Composite Airfoils, Cold Reg. Sci. Technol., 2013, 87(3), p 47–58.

[26] H. Habibi, L. Cheng, H. Zheng, V. Kappatos, C. Selcuk, and T.-H. Gan, A Dual De-Icing System for Wind Turbine Blades Combining High-Power Ultrasonic Guided Waves and Low-Frequency Forced Vibrations, Renew. Energy, 2015, 83(11), p 859–870.

[27] C. Soutis, Introduction: Engineering Requirements for Aerospace Composite Materials, *Polymer Composites in the Aerospace Industry*, 1st ed., Woodhead Publishing, 2015 (Cambridge), p 1.

[28] P. Brøndsted, H. Lilholt, and A. Lystrup, Composite Materials for Wind Power Turbine Blades, Annu. Rev. Mater. Res., 2005, 35(1), p 505–538.

[29] N. Buckney, A. Pirrera, S.D. Green, and P.M. Weaver, Structural Efficiency of a Wind Turbine Blade, Thin-Walled Struct., 2013, 67(1), p 144–154.

[30] A.J. Brunner, Fracture Mechanics Characterization of Polymer Composites for Aerospace Applications, *Polymer Composites in the Aerospace Industry*, 1st ed., Woodhead Publishing, 2015 (Cambridge), p 191-194.

[31] S. Han, and D.D.L. Chung, Increasing the Through-Thickness Thermal Conductivity of Carbon Fiber Polymer–Matrix Composite by Curing Pressure Increase and Filler Incorporation, Compos. Sci. Technol., 2011, 71(16), p 1944–1952.

[32] P. Fauchais, and G. Montavon, Thermal and Cold Spray: Recent Developments, Key Eng. Mater., 2008, 384(6), p 1–59.

[33] P. Vuoristo, Thermal Spray Coating Processes, *Comprehensive Materials Processing*, 4th ed., Elsevier Inc., 2014 (Oxford), p 238-239.

[34] L.-M. Berger, Coatings by Thermal Spray, *Comprehensive Materials Processing*, 4th ed., Elsevier Inc., 2014 (Oxford), p 473-475.

[35] R. Gonzalez, A. McDonald, and P. Mertiny, Damage Detection Method for Fiber-Reinforced Polymer Composites Using Al-12Si FlameSsprayed Coatings, SAMPE 2014, June 2-5, 2014 (Seattle, Washington, USA), Society for the Advancement of Material and Process Engineering Conference, 2014, p 1–9.

[36] J.-M. Lamarre, P. Marcoux, M. Perrault, R.C. Abbott, and J.-G. Legoux, Performance Analysis and Modeling of Thermally Sprayed Resistive Heaters, J. Therm. Spray Technol., 2013, 22(6), p 947–953.

[37] T. Samerjai, N. Tamaekong, K. Wetchakun, V. Kruefu, C. Liewhiran, C. Siriwong, A. Wisitsoraat, and S. Phanichphat, Flame-Spray-Made Metal-Loaded Semiconducting Metal Oxides Thick Films for Flammable Gas Sensing, Sensors Actuators B Chem., 2012, 171(10), p 43–61.

[38] M. Prudenziati, Development and the Implementation of High-Temperature Reliable Heaters in Plasma Spray Technology, J. Therm. Spray Technol., 2008, 17(2), p 234–243.

[39] F. Robitaille, M. Yandouzi, S. Hind, and B. Jodoin, Metallic Coating of Aerospace Carbon/Epoxy Composites by the Pulsed Gas Dynamic Spraying Process, Surf. Coatings Technol., 2009, 203(19), p 2954–2960.

[40] R. Gonzalez, A. McDonald, and P. Mertiny, Effect of Flame-Sprayed Al–12Si Coatings on the Failure Behaviour of Pressurized Fibre-Reinforced Composite Tubes, Polym. Test., 2013, 32(8), p 1522–1528.

[41] N. Huonnic, M. Abdelghani, P. Mertiny, and A. McDonald, Deposition and Characterization of Flame-Sprayed Aluminum on Cured Glass and Basalt Fiber-Reinforced Epoxy Tubes, Surf. Coatings Technol., 2010, 205(3), p 867–873.

[42] Oerlikon Metco, "Material Product Data Sheet: Nickel-20 wt.% Chromium (Ni-20Cr) Powders for Thermal Spray", Oerlikon Metco, Westbury, USA, 2013, p 1-5.

[43] Oerlikon Metco, "Material Product Data Sheet: Nickel Chromium Aluminum Yttrium (NiCrAlY) Powder for Thermal Spray", Oerlikon Metco, Westbury, USA, 2014, p 1-6.

[44] S. Vinayak, H.P. Vyas, and V.D. Vankar, Microstructure and Electrical Characteristics of Ni–Cr Thin Films, Thin Solid Films, 2007, 515(18), p 7109–7116.

[45] S. Vinayak, H.P. Vyas, K. Muraleedharan, and V.D. Vankar, Ni–Cr Thin Film Resistor Fabrication for Gas Monolithic Microwave Integrated Circuits, Thin Solid Films, 2006, 514(1), p 52–57.

[46] P. Jain, S. Raj, and K. Hemker, Characterization of NiCrAlY Coatings for a High Strength, High Conductivity GRCop-84 Copper Alloy, Acta Mater., 2007, 55(15), p 5103–5113.

[47] ”Standard Test Method for Ignition Loss of Cured Reinforced Resin", ASTM D2584-11, ASTM, 2011, p 1-3.

[48] A. Kaw, *Mechanics of Composite Materials*, 2nd ed., Taylor & Francis Group, 2006 (Boca Raton, FL), p 205-207.

[49] H. Yu, D. Heider, and S. Advani, Prediction of Effective Through-Thickness Thermal Conductivity of Woven Fabric Reinforced Composites with Embedded Particles, Compos. Struct., 2015, 127(11), p 132–140.

[50] Spraying Systems Co., “Industrial Hydraulic Spray Products”, Spraying Systems Co., Wheaton, USA, 2013, p E4. H. S.

[51] L. M. Jiji, *Heat Conduction*, 3rd ed., John Wiley & Sons, Inc., 2012 (New York), p 36-38.

[52] J. P. Holman, *Heat Transfer*, 10th ed., McGraw-Hill Higher Education, 2010 (New York), p 222-230.

[53] A. McDonald, B. Bschaden, E. Sullivan, and R. Marsden, Mathematical Simulation of the Freezing Time of Water in Small Diameter Pipes, Appl. Therm. Eng., 2014, 73(1), p 140–151.

[54] W. Rohsenow, J. Hartnett, and Y. Cho, *Handbook of Heat Transfer*, 3rd ed., McGraw-Hill, 1998 (New York), p 6.16-6.19.

[55] Carslaw and J.C. Jaeger, *Conduction of Heat in Solids*, 2nd ed., Clarendon Press, 1986 (Oxford), p 282-296.

[56] G.M. Nelson, J.A. Nychka, and A.G. McDonald, Structure, Phases, and Mechanical Response of Ti-Alloy Bioactive Glass Composite Coatings, Mater. Sci. Eng. C, 2014, 36(1), p 261–276.

[57] D. C. Montgomery, *Design and Analysis of Experiments*, 8th ed., John Wiley & Sons, Inc., 2013 (New York, NY.), p 450-451.

[58] L. Liu, B.-M. Zhang, D.-F. Wang, and Z.-J. Wu, Effects of Cure Cycles on Void Content and Mechanical Properties of Composite Laminates, Compos. Struct., 2006, 73(3), p 303–309.

[59] J.-M. Tang, W.I. Lee, and G.S. Springer, Effects of Cure Pressure on Resin Flow, Voids, and Mechanical Properties, J. Compos. Mater. , 1987, 21(5), p 421–440.

[60] P. Olivier, J.P. Cottu, and B. Ferret, Effects of Cure Cycle Pressure and Voids on Some Mechanical Properties of Carbon/Epoxy Laminates, Composites, 1995, 26(7), p 509–515.

[61] A. Goullieux, J. Pain, D.P. Verne, and L. Eproad, Ohmin Heating, *Emerging Technologies for Food Processing*, 2nd ed., Elsevier Academic Press, 2014 (Amsterdam), p 399–400.

[62] A.A. Al-Aql, Electrical Resistivity Measurements in Ni–Cr Alloys, Mater. Des., 2003, 24(7), p 547–550.

[63] A.M. Rana, A.F. Khan, A. Abbas, and M.I. Ansari, Electrical Resistivity Behavior in Ni–25 At.% Cr Alloy, Mater. Chem. Phys., 2003, 80(1), p 228–231.

[64] P.S. Liu, T.F. Li, and C. Fu, Relationship between Electrical Resistivity and Porosity for Porous Metals, Mater. Sci. Eng. A, 1999, 268(1-2), p 208–215.

[65] L.D. Harvey, The Potential of Wind Energy to Largely Displace Existing Canadian Fossil Fuel and Nuclear Electricity Generation, Energy, 2013, 50(1), p 93–102.

[66] A. Ilinca, E. McCarthy, J.-L. Chaumel, and J.-L. Rétiveau, Wind Potential Assessment of Quebec Province, Renew. Energy, 2003, 28(12), p 1881–1897.

[67] American Society of Heating, Refrigerating and Air-Conditioning Engineers Inc., *ASHRAE Handbook – Fundamentals*, I-P ed., ASHRAE, 2005 (Atlanta), p 25.2-25.15.

[68] A. Culver, and A. Monahan, The Statistical Predictability of Surface Winds over Western and Central Canada, J. Clim., 2013, 26(21), p 8305–8322.

[69] Y. Çengel and J. Cimbala, *Fluid Mechanics: Fundamentals and Applications*, 3rd ed., McGraw-Hill, 2014 (New York), p 557–558.

[70] T. L. Bergman, A. S. Lavine, F. P. Incropera, and D. P. DeWitt, *Fundamentals of Heat and Mass Transfer*, 7th ed., John Wiley & Sons, Inc., 2011 (New York), p 408.

[71] D.W. James, The Thermal Diffusivity of Ice and Water between -40°C and + 60°C, J. Mater. Sci., 1968, 3(5), p 540–543.

[72] M. Necati Özişik, *Heat Conduction*, 2nd ed., John Wiley & Sons, Inc., 1993 (New York), p 292-297.